THE UNIVERSITY *of* EDINBURGH

Phase Stability of Titanium Alloys: A First Principles Study

Bengt Tegner

Doctor of Philosophy
The University of Edinburgh
2014

Lay Summary

One of the central questions of metallurgy is which structure a certain alloy will adopt as a function of pressure and temperature. This question can be traced back all the way from Antiquity, via the first steel makers of the Middle Ages and the metallurgists of the 19th century, to the present day. Experiences drawn from centuries of alloy making have given rise to well-established rules of thumb for alloy development and detailed phase diagrams for equilibrium conditions.

However, predicting the structure and properties of a single alloy at a given temperature is remarkably difficult. This thesis attempts to answer this question by solving the quantum mechanical equations describing these alloys using high-performance computers.

We find that in the case of titanium alloys, chromium and vanadium stabilise the ductile cubic phase, while aluminium and scandium destabilise it. The strength of this stabilising effect is directly proportional to the additional valence electrons present in the alloying element.

Using these results, we can construct new phase diagrams and equations of state for these alloys. This gives us a theoretical confirmation for established rules of thumb and provides us with new guidelines and insights when designing new alloys.

Abstract

One of the central questions of materials science is which crystallographic structure a certain alloy or compound will adopt as a function of elemental composition, pressure and temperature. This question can be traced back all the way from the Bronze Age via the first steel makers of the Middle Ages and the metallurgists of the 19th century to the present day. Experiences drawn from centuries of alloy making have given rise to well-established rules of thumb for alloy development and detailed phase diagrams for equilibrium conditions.

However, a rigorous theory for single-phase alloys out of equilibrium is less well established. This study employs state-of-the-art electronic structure calculations based on density functional theory to tackle this problem. This method employs a reformulation of quantum mechanics to solve the many-body Schrödinger equation that describes the system. In our case, the system is a titanium alloy, where titanium is substitutionally alloyed with elements such as aluminium, chromium, vanadium and molybdenum.

We find that chromium and vanadium stabilise the β phase, while scandium destabilises it. The strength of this effect is directly proportional to the additional d-electrons present in the alloying element. The effect appears to be additive, and the positional effects of the alloying atoms appear to be small.

Using the results from the calculations we can construct new phase diagrams and equations of state for these alloys. This gives us a theoretical confirmation for established rules of thumb and provides us with new insights when constructing new alloys.

Declaration

Except where otherwise stated, the research undertaken in this thesis was the unaided work of the author. Where the work was done in collaboration with others, a significant contribution was made by the author. Exceptions are the VCA calculations in chapter 4, which were performed by Linggang Zhu [Tegner 12], and the experimental data in chapter 5, which were obtained by MacLeod and coworkers [MacLeod 12].

Bengt Tegner
May 2014

Acknowledgements

I would like to take this moment to thank all those who have helped me in the course of this work. In particular, the following:

Prof. Graeme Ackland for his guidance, assistance and encouragement.

Dr. Carsten Siemers for coordinating the MaMiNa network.

The European Union Seventh Framework Programme for Research (FP7) for financial support.

My office mates Con Healy and Dominic Russell, for creating such a nice working atmosphere and bringing me endless cups of tea.

And last but not least, to Anne, for her love and support throughout, and to whom this thesis is dedicated.

Contents

List of Figures

List of Tables

Chapter 1

Introduction

1.1 Background

The science of metallurgy can be traced back into Antiquity, with weapons and armour being made of bronze, via the steel makers of the Middle Ages to the development of modern stainless steels of the 19th century. Gus Hart wrote the following in a recent overview in Nature [Hart 12]:

> Early civilizations began alloying copper with arsenic, tin or zinc nearly 6,000 years ago [Sass 98], ushering in the Bronze Age. Even when more-abundant iron became a mainstay during the Iron Age, substitutional alloys of copper – in which some of the copper atoms were replaced with atoms of a different metal – were superior materials. So Roman foot soldiers were equipped with wrought-iron weapons, whereas Roman officers had swords made of bronze. Similarly, at the turn of the twentieth century, French scientists developed a steel that substituted some iron with vanadium. This alloy, which had three times the tensile strength of competing steels, became an essential ingredient of the venerable Ford Model T (and of early French luxury cars).

Despite the long history of alloy making, predicting the properties of a particular alloy from the composition alone is a remarkably difficult. Alloy designers have some well-established rules of thumb, derived from work by pioneers such as William Hume-Rothery [Hume-Rothery 34, Hume-Rothery 50] and David

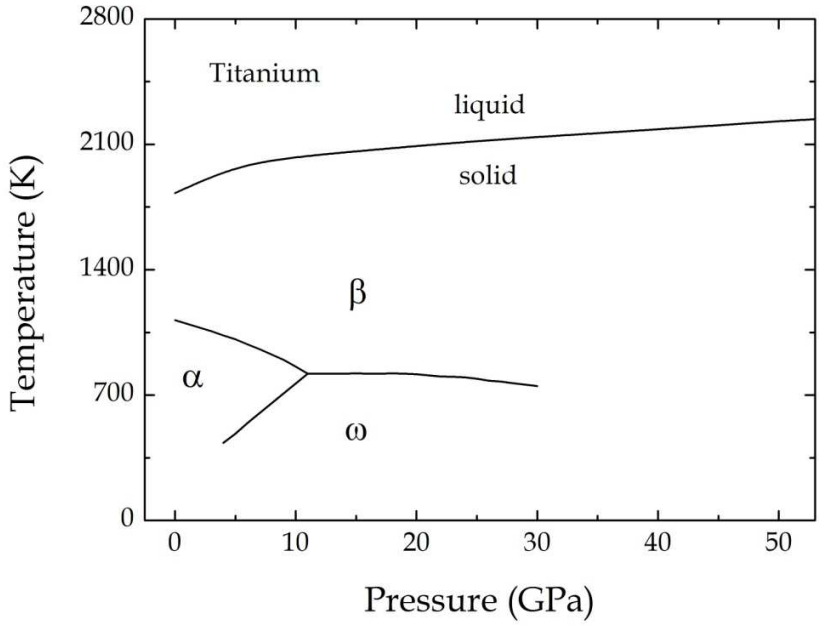

Figure 1.1: Sketch of the phase diagram of titanium as a function of temperature and pressure, showing the α, β, and ω phases. (Figure adapted from [Velisavljevic 12].)

Pettifor [Pettifor 70, Pettifor 84]. However, a well-grounded, consistent theory is still lacking. This represents a major bottle-neck when designing and developing new materials.

This thesis will attempt to address this issue using state-of-the-art electronic structure calculations. This method employs high-performance computers to solve the quantum mechanical equations governing the system. The advantage of using this method is that it is quite accurate, and being a so-called *ab-initio* method, it does not rely on any empirical input. That said, the main downside of this method is that it can be very computationally demanding.

The main alloys we will study here are titanium alloys. Titanium and its alloys plays a major role in several technological applications, particularly in the aerospace industry [Boyer 96], due to a favourable combination of high strength, low weight, and excellent resistance to corrosion.

Pure titanium metal crystallises in three distinct crystal structures: α, β, and ω. A sketch of the phase diagram, published by Velisavljevic *et al.* [Velisavljevic 12], is shown in figure 1.1, showing the three main phases.

At room temperature and ambient pressure, the α-phase is formed. This is a hexagonal-close-packed (hcp) structure with space group $P6_3/mmc$, two atoms in the primitive unit cell, and a c/a-ratio of ~ 1.59. At higher temperature, about 1150 K, the β phase is formed. This is a body-centred cubic structure with space group $Im3m$ and one atom in the primitive unit cell. On compression, titanium transforms into the ω phase, a hexagonal structure with space group $P6/mmm$, three atoms in the primitive unit cell and a c/a-ratio of ~ 0.6.

Adding alloying elements such as aluminium, chromium and vanadium is known to change the phase diagram outlined in the figure above by stabilising a particular phase. One of the aims of this study is to quantify the phase-stabilising behaviour of commonly used alloying elements and identify the electronic driving forces behind it.

1.2 Thesis Outline

This thesis is arranged in the following way. Chapter 1 is the introduction. Chapter 2 will give a brief outline of the theory underpinning the calculations. Chapters 3, 4, 5 and 6 will describe the main results of this work. Chapter 7 will summarise the main conclusions.

Chapter 2

Theory

> Then I would have felt sorry for the dear Lord. The theory is correct.
> — Albert Einstein

This chapter outlines the theory underpinning the calculations on which the rest of this thesis is based.

2.1 Quantum Mechanics

Matter is made up of atoms bound together by electrons, which implies that any fundamental theory of matter has to be one involving electrons. The basic equation describing a system of electrons is the Schrödinger equation, which can be written as follows:

$$\hat{H}\mathbf{\Psi} = E\mathbf{\Psi}, \tag{2.1}$$

where $\hat{H} = (\hat{T} + \hat{V})$ is the Hamiltonian of the system and E is the total energy of the system.

2.1.1 The Hydrogen Atom

For the special case of a single electron orbiting a central nucleus, the Schrödinger equation can be solved exactly. Setting $\hat{V}$ to be the classical Coulomb potential in the Hamiltonian above, the Schrödinger equation now has the following form in spherical coordinates:

$$\left(-\frac{\hbar^2}{2\mu}\nabla^2 - \frac{Ze^2}{4\pi\varepsilon_0 r}\right)\Psi(r,\theta,\phi) = E\Psi(r,\theta,\phi), \tag{2.2}$$

with the solution

$$\Psi(r,\theta,\phi) = R_{n,l}(r)\mathrm{P}_l^m(\cos(\theta))\mathrm{e}^{\mathrm{i}m\phi}, \tag{2.3}$$

and the energy eigenvalues

$$E_n = -\frac{\mu Z^2 e^4}{2\hbar^2(4\pi\varepsilon_0)^2}\left(\frac{1}{n^2}\right), \tag{2.4}$$

where n, l and m are the principal, orbital and magnetic quantum numbers. For more details of this solution, see for example Haken and Wolf, [Haken 05].

2.1.2 The Many-Electron Problem

Furthermore, for a system of interacting electrons moving in a solid, the many-body Hamiltonian can be expressed as the following

$$\hat{H} = \sum_{i=1}^{N}\left(-\frac{\hbar^2}{2m_e}\nabla_i^2 + V_{ion}(\mathbf{r}_i) + V_{e-e}(\mathbf{r}_i)\right), \tag{2.5}$$

where $V_{ion}(\mathbf{r}_i)$ is the potential of the atomic nuclei at fixed positions $\mathbf{R}$,

$$V_{ion}(\mathbf{r}_i) = \sum_{\mathbf{R}} -\frac{Ze^2}{4\pi\varepsilon_0|\mathbf{R}-\mathbf{r}_i|}, \tag{2.6}$$

and $V_{e-e}(\mathbf{r}_i)$ is the electron-electron interaction, given by

$$V_{e-e}(\mathbf{r}_i) = \frac{1}{2}\sum_{i\neq j}\frac{e^2}{4\pi\varepsilon_0|\mathbf{r}_i-\mathbf{r}_j|}. \tag{2.7}$$

In general, it is not possible to solve this equation for any system beyond simple atoms, due to the difficult nature of the electron-electron interaction. One possible approach is to employ quantum Monte Carlo methods [Needs 10, Nemec 10, Booth 13], which are extremely accurate, but unfortunately also prohibitively expensive. For extended systems like metal alloys, a different approach is currently needed.

2.2 Density Functional Theory

Hohenberg and Kohn [Hohenberg 64] proved that the total energy of a system, including many-body effects, in the presence of a static external potential is a unique functional of the charge density $n(\mathbf{r})$. The minimum value of this total energy functional is the ground state energy of the system. The electronic charge density which yields this minimum is then the exact single particle ground state energy.

It was then shown by Kohn and Sham [Kohn 65] that it is possible to replace the many electron problem by an exactly equivalent set of self-consistent one-electron equations. The total energy functional can be written as a sum of several terms, given by

$$E[n(\mathbf{r})] = \int V_{ion}(\mathbf{r})n(\mathbf{r})\mathrm{d}\mathbf{r} + \frac{1}{2}\iint \frac{n(\mathbf{r})n(\mathbf{r}')}{4\pi\varepsilon_0|\mathbf{r}-\mathbf{r}'|}\mathrm{d}\mathbf{r}\mathrm{d}\mathbf{r}' + G[n(\mathbf{r})], \tag{2.8}$$

where the first term is the classical Coulomb interaction between the electrons and the external potential $V_{ion}(\mathbf{r})$ due to the ions, now expressed using an integral over the density, the second term is the self interaction between electrons and other electrons, also expressed using an integral over the density. The third term, $G[n(\mathbf{r})]$, contains all the many body effects of exchange and correlation, plus the single particle kinetic energy, and is given by

$$G[n(\mathbf{r})] = T_s[n(\mathbf{r})] + E_{XC}[n(\mathbf{r})], \tag{2.9}$$

where $T_s[n(\mathbf{r})]$ is the kinetic energy of a system of non-interacting electrons with density $n(\mathbf{r})$ and $E_{XC}[n(\mathbf{r})]$ is the energy of exchange and correlation of an interacting system. Unfortunately, there is no simple expression for the exchange and correlation term $E_{XC}[n(\mathbf{r})]$ and the Hohenberg-Kohn theorem gives no clue to what the expression might be. However, several approximations exist, some of which will be discussed in the following sections.

That said, given an expression for $E_{XC}[n(\mathbf{r})]$, the solution can be found by solving the Schrödinger-like Kohn-Sham equations for a set of non-interacting particles moving in an effective potential $V_{KS}(\mathbf{r})$:

$$\left(-\frac{\hbar^2}{2m}\nabla^2 + V_{KS}(\mathbf{r})\right)\psi_i(\mathbf{r}) = \mathcal{E}_i\psi_i(\mathbf{r}), \tag{2.10}$$

where the effective potential $V_{KS}(\mathbf{r})$ is given by

$$V_{KS}(\mathbf{r}) = V_{ion}(\mathbf{r}) + V_H(\mathbf{r}) + V_{XC}(\mathbf{r}), \tag{2.11}$$

where $V_{ion}(\mathbf{r})$ is given by Eq. 2.6, $V_H(\mathbf{r})$ is given by

$$V_H(\mathbf{r}) = \int \frac{n(\mathbf{r}')}{4\pi\varepsilon_0|\mathbf{r} - \mathbf{r}'|}\mathrm{d}\mathbf{r}', \tag{2.12}$$

and $V_{XC}(\mathbf{r})$ is given by

$$V_{XC}(\mathbf{r}) = \frac{\delta E_{XC}[n(\mathbf{r})]}{\delta n(\mathbf{r})}. \tag{2.13}$$

The charge density $n(\mathbf{r})$ is then obtained by taking the square of the Kohn-Sham wavefunctions $\psi_i(\mathbf{r})$

$$n(\mathbf{r}) = \sum_i^N \psi_i^*(\mathbf{r})\psi_i(\mathbf{r}), \tag{2.14}$$

where N is the total number of electrons.

2.2.1 The Local Density Approximation

The first approximation to $E_{XC}[n(\mathbf{r})]$ was given by Kohn and Sham [Kohn 65], followed by expressions by Hedin and Lundqvist [Hedin 71] and others, which all make use of the fact that the there are known expressions for the exchange correlation energy for a uniform electron gas. This yields the so called *local density approximation*, or (LDA). Assuming the electron density to be uniform locally, we can write $E_{XC}^{LDA}[n(\mathbf{r})]$ as

$$E_{XC}^{LDA}[n(\mathbf{r})] = \int n(\mathbf{r})\epsilon_{xc}[n(\mathbf{r})]\mathrm{d}\mathbf{r}, \tag{2.15}$$

where $\epsilon_{xc}(n)$ is the exchange correlation energy of a uniform electron gas of density n. This was later generalised to spin systems by Gunnarsson and Lundqvist [Gunnarsson 76], forming the *local spin density approximation*, or LSDA.

The most commonly used LDA parametrisation is the one by Perdew and Zunger [Perdew 81], which is based on quantum Monte Carlo calculations on uniform electron gases at different densities by Ceperley and Alder [Ceperley 80].

2.2.2 The Generalised Gradient Approximation

For systems with rapidly varying charge density, the local density approximation might fail. A commonly used generalisation is to take not only the local density into account, but also the gradient of said density. This yields the *generalised density approximation*, or GGA, which can be expressed as

$$E_{XC}^{GGA}[n(\mathbf{r})] = \int n(\mathbf{r})\epsilon_{xc}[n(\mathbf{r})]F_{xc}[n(\mathbf{r}), |\nabla n(\mathbf{r})|]\mathrm{d}\mathbf{r}. \tag{2.16}$$

where F_{xc} is known as the enhancement factor. Several GGA parametrisations exist, and the GGA parametrisation commonly used for solid state systems, and also used throughout this thesis unless otherwise specified, is the one by Perdew, Burke and Ernzerhof [Perdew 96], (PBE-GGA), which is an improved version of an earlier parametrisation by Perdew and Wang [Perdew 92a], (PW91-GGA), which itself is based on an analytic fit to the Monte Carlo data of Ceperley and Alder [Perdew 92b].

2.3 Periodic Boundary Conditions and Plane Wave Basis Sets

For crystalline systems, due to the periodic nature of the ionic potential, it is natural to use periodic boundary conditions, where the period is the crystal unit cell length. Using Bloch's theorem, the Kohn-Sham wavefunctions describing an electron moving in said potential can therefore be expressed as

$$\psi_i(\mathbf{r}) = f_i(\mathbf{r}) \exp(\mathrm{i}\mathbf{k} \cdot \mathbf{r}), \tag{2.17}$$

where $f_i(\mathbf{r})$ can be written as sum of plane waves whose wave vectors $\mathbf{k}$ correspond to reciprocal crystal lattice vectors $\mathbf{G}$, given by

$$f_i(\mathbf{r}) = \sum_m c_{i,m}(\mathbf{k}) \exp(\mathrm{i}\mathbf{G} \cdot \mathbf{r}), \tag{2.18}$$

which means that the wavefunctions $\psi_i(\mathbf{r})$ can be expressed using a discrete sum of plane waves. In practice, the number of plane waves, or completeness of the

basis set, is controlled by the plane-wave cutoff E_{cut}, given by

$$E_{cut} = \frac{\hbar^2}{2m}|\mathbf{k} + \mathbf{G_{cut}}|^2. \tag{2.19}$$

2.4 Pseudopotentials

The Kohn-Sham equations outlined above can be further simplified by only treating the valence electrons explicitly. This reduces the computational cost by reducing the number of plane waves needed, due to not having to describe the rapidly oscillating wavefunctions near the core. This approach, which is usually called the pseudopotential approximation, removes the core electrons and replaces the ionic potential $V_{ion}(\mathbf{r})$ with a weaker potential $V_{PSP}(\mathbf{r})$. Inserting this approximation into Eq. 2.10 above yields

$$\left(-\frac{\hbar^2}{2m}\nabla^2 + V_{PSP}(\mathbf{r}) + V_H(\mathbf{r}) + V_{XC}(\mathbf{r})\right)\phi_i(\mathbf{r}) = \mathcal{E}_i\phi_i(\mathbf{r}), \tag{2.20}$$

where $\phi_i(\mathbf{r})$ are the corresponding pseudo-wavefunctions.

2.4.1 Pseudopotential Construction

A pseudopotential can be constructed in several ways, including empirical fitting to experimental band structures. The present approach, first proposed by Hamann, Schlüter and Chiang [Hamann 79], with improvements by Kleinman and Bylander [Kleinman 82], Rappe *et al.* [Rappe 90], and Troullier and Martins [Troullier 91], is to construct the pseudopotential from first principles, starting from a solution to the Schrödinger equation only.

Given a solution ψ_i at energy ε_i^{AE} to the Schrödinger equation for the full all-electron potential $V_{AE}(r)$, a core cutoff radius r_c is chosen for each angular momentum l and a special set of smooth pseudo-wavefunctions $\phi_l(\mathbf{r})$ are constructed inside $r < r_c$, matching ψ_l at $r = r_c$, and matching $\varepsilon_i^{AE} = \varepsilon_i^{PS}$, using a smooth local potential $V_{loc}(r)$ which approaches $V_{AE}(r)$ outside $r > r_c$.

These pseudo-wavefunctions $\phi_l(\mathbf{r})$ can be expressed as (using atomic units):

$$\phi_l(\mathbf{r}) = \sum_{i=1}^{n} \alpha_i j_l(q_i r), \tag{2.21}$$

with the condition

$$\frac{j_l^{'}(q_i r_c)}{j_l(q_i r_c)} = \frac{\psi_l^{'}(r_c)}{\psi_l(r_c)}, \tag{2.22}$$

where $j_l(q_i r)$ are spherical Bessel functions with $(i-1)$ zeros between $r = 0$ and $r = r_c$, and $\psi_l(r)$ is the all-electron wavefunction. Lagrange multipliers are the used to modify the first four coefficients α_i to ensure normalisation of $\phi_l(\mathbf{r})$; and to ensure continuity of its first two derivatives at $r = r_c$. The rest of the coefficients α_i are determined by minimising the kinetic energy beyond the cutoff vector q_c:

$$\Delta E_k(\alpha_i, q_c) = -\int_0^{\infty} \phi_l^*(\mathbf{r})\nabla^2\phi_l(\mathbf{r})\mathrm{d}\mathbf{r} - \int_0^{q_c} q^2|\phi_l(\mathbf{q})|^2\mathrm{d}\mathbf{q}, \tag{2.23}$$

where $\phi_l(\mathbf{q})$ is the Fourier transform of $\phi_l(\mathbf{r})$ and q_c is chosen to match q_n in equation 2.21 above.

The pseudopotential $V_l^{PS}(r)$ is then obtained by inverting the Schrödinger equation given the optimised $\phi_l(\mathbf{r})$.

The final pseudopotential can then be written as

$$V_{PS}^{HSC} = V_{loc}(r) + \sum_{lm} |Y_{lm}\rangle \Delta V_l^{HSC}(r) \langle Y_{lm}|, \tag{2.24}$$

where Y_{lm} are spherical harmonics, $V_{loc}(r)$ is the smooth local potential, approaching $V_{AE}(r)$ outside $r > r_c$, and $\Delta V_l^{HSC}(r) = V_{loc}(r) - V_l^{HSC}$ for $r < r_c$.

In practice, one has to:

1. Choose r_c small enough to ensure transferability but also large enough to be bigger than the physical core radius.

2. Choose a large enough number of spherical Bessel functions, typically ten or more.

3. Tune q_c for a given r_c to ensure that the convergence error in ΔE_k is below a given tolerance.

Details of this optimisation scheme can be found in the work by Lin *et al.* [Lin 93].

The resulting optimised pseudopotentials have the following properties by construction:

1. The AE and the PSP eigenvalues agree for a chosen reference atomic configuration.
2. The AE and the PSP wavefunctions agree beyond $r = r_c$.
3. The integrated charge densities $\int \psi_i^* \psi_i \mathrm{d}r$ and $\int \phi_i^* \phi_i \mathrm{d}r$ agree for $r > r_c$, (norm conservation).
4. The logarithmic derivatives of both the AE and the PSP wavefunctions and their first energy derivatives agree for $r > r_c$.

where properties (3) and (4) above makes sure that the electrostatic potential and scattering properties of the real ion core are correctly reproduced by the resulting pseudo-ion.

However, the generation scheme above may yield pseudopotentials which are comparatively "hard" in the sense that a large number of Fourier components (high cutoff energy) are required for an accurate representation [Kerker 80, Bachelet 82]. This is a particular problem in the case of first-row transition elements.

Relaxing the strict requirement for norm-conservation, first introduced by D. Vanderbilt [Vanderbilt 90], yields the so called "ultrasoft" pseudopotential, which allows the pseudo-wavefunctions to be as soft as possible within the core region, and allows the cutoff energy to be reduced accordingly. However, the trade-off is that the Kohn-Sham equations acquire additional terms due to this relaxed condition, resulting in an increase in computational complexity.

2.4.2 Ultrasoft Pseudopotentials Construction

An ultrasoft pseudopotential can be written as:

$$V_{PSP}^{US} = V_{loc}^{ion} + V_{NL}, \tag{2.25}$$

where the local part V_{loc}^{ion} is given by $V_{loc}^{ion} \equiv V_{loc} - V_H - V_{XC}$, and a non-local part, given by

$$V_{NL} = \sum_{nm} D_{nm}^0 |\beta_n\rangle\langle\beta_m|, \tag{2.26}$$

where the functions β_n as well as the coefficients D_{nm}^0, characterise this type of pseudopotential, and differ for different atomic species. Here, β_n is an angular

momentum eigenfunction times a radial function which vanishes outside the core region. The indices m and n run over the total number of such beta-functions and will vary depending on the number of reference energies chosen per angular momentum.

Moreover, the electron charge density $n(\mathbf{r})$ is now given by the expression

$$n(\mathbf{r}) = \sum_i \left[|\phi_i(\mathbf{r})|^2 + \sum_{nm} Q_{nm}(\mathbf{r}) \langle \phi_i | \beta_n \rangle \langle \beta_m | \phi_i \rangle \right], \tag{2.27}$$

where $\phi_i(\mathbf{r})$ are the pseudo-wavefunctions as before and $Q_{nm}(\mathbf{r})$ are new charge augmentation functions, strictly localised inside the core region, introduced due to relaxing the norm-conservation requirement (3) above.

Additionally, the relaxation of the norm-conservation requirement also gives rise to a generalised orthonormality condition, given by

$$\langle \phi_i | \hat{S} | \phi_j \rangle = \delta_{ij}, \tag{2.28}$$

where $\hat{S}$ is an Hermitian overlap operator, given by

$$\hat{S} = 1 + \sum_{nm} q_{nm} |\beta_n\rangle \langle \beta_m|, \tag{2.29}$$

where the coefficients q_{nm} are obtained by integrating the augmentation functions $Q_{nm}(r)$, given by

$$q_{nm} = \int Q_{nm}(r) \mathrm{d}r. \tag{2.30}$$

The Kohn-Sham equations Eq. 2.20 now become a generalised eigenvalue problem, given by

$$\left(-\frac{\hbar^2}{2m} \nabla^2 + V_{loc}^{eff}(\mathbf{r}) + \sum_{nm} D_{nm} |\beta_n\rangle \langle \beta_m| \right) \phi_i(\mathbf{r}) = \mathcal{E}_i S \phi_i(\mathbf{r}), \tag{2.31}$$

where $V_{loc}^{eff}(\mathbf{r})$ is the screened effective local potential, given by

$$V_{loc}^{eff}(\mathbf{r}) = V_{loc}^{ion}(\mathbf{r}) + \int \frac{n(\mathbf{r}')}{|\mathbf{r} + \mathbf{r}'|} \mathrm{d}\mathbf{r}' + V_{XC}(\mathbf{r}), \tag{2.32}$$

where the terms arising from the augmentation functions Q_{nm} have been grouped

into the non-local part by introducing the new coefficients D_{nm}, given by

$$D_{nm} = D^0_{nm} + \int V^{eff}_{loc}(\mathbf{r}) Q_{nm}(\mathbf{r}) \mathrm{d}\mathbf{r}. \tag{2.33}$$

As in the previous case, we start from a solution to the all-electron Schrödinger equation to obtain the potential $V_{AE}(r)$. Then, for each angular momentum l, a number of reference energies $\varepsilon_{l\tau}$ are chosen, covering the valence states. For each $\varepsilon_{l\tau}$, a solution $|\psi_n\rangle$ is obtained, given by the equation

$$(T + V_{AE})|\psi_n\rangle = \varepsilon_n |\psi_n\rangle. \tag{2.34}$$

Here n is a composite index $n = l\tau$, and T is the kinetic energy operator $T = -\frac{1}{2}\nabla^2$. Despite the fact that ψ_n are not generally normalisable, we adopt the notation $\langle\psi_n|\psi_m\rangle_R$ to denote the integral of $\psi^*_n(\mathbf{r})\psi_m(\mathbf{r})$ inside the sphere of radius R.

Next, given a cut off radius r_{cl} for each wavefunction ψ_n above, we construct a corresponding pseudo-wavefunction ϕ_n, only subject to the constraint that it joins ψ_n smoothly at $r = r_{cl}$. Also, a local potential $V_{loc}(r)$ is generated so that it matches V_{AE} smoothly at a separate cut off radius $r = r^{loc}_c$. Furthermore, a diagnostic radius R is chosen such that it is larger than both r_{cl} and r^{loc}_c. This allows us to form a set of purely local pseudo-wavefunctions $|\chi_n\rangle$, given by

$$|\chi_n\rangle = (\varepsilon_n - T - V_{loc})|\phi_n\rangle, \tag{2.35}$$

which vanish outside R where $V_{loc} = V_{AE}$ and $\phi_n = \psi_n$. The matrix of inner products between the wavefunction $|\phi_n\rangle$ at energy ε_n and the wavefunction $|\chi_m\rangle$ at energy ε_m is now well-defined, and given by

$$B_{nm} = \langle\phi_n|\chi_m\rangle. \tag{2.36}$$

We can now form the quantites V^{ion}_{loc}, D^0_{nm}, $Q_{nm}(\mathbf{r})$ and $\beta_n(\mathbf{r})$ needed to fully specify the ultrasoft pseudopotential. The charge augmentation functions Q_{nm} and the beta-projectors $|\beta_n\rangle$ are given by

$$Q_{nm}(r) = \psi_n(r)^*\psi_m(r) - \phi_n(r)^*\phi_m(r), \tag{2.37}$$

and

$$|\beta_n\rangle = \sum_m \frac{|\chi_m\rangle}{\langle\chi_m|\phi_n\rangle}, \tag{2.38}$$

respectively, where $|\beta_n\rangle$ are duals to $|\phi_n\rangle$ and form the projectors of V_{NL}.

Finally, the coefficients D^0_{nm} and the local potential V^{ion}_{loc} are formed using a descreening procedure, where D^0_{nm} is given by

$$D^0_{nm} = B_{nm} + \varepsilon_m q_{nm} - \int V_{loc}(\mathbf{r}')n(\mathbf{r}')\mathrm{d}\mathbf{r}', \tag{2.39}$$

where $q_{nm} = \int Q_{nm}(r)\mathrm{d}r$ as above, ε_m is obtained from the expression

$$B_{nm} - B^*_{mn} = (\varepsilon_n - \varepsilon_m)Q_{nm}, \tag{2.40}$$

which vanishes when $Q_{nm} = 0$, and V^{ion}_{loc} is given by

$$V^{ion}_{loc}(r) = V_{loc}(r) - \int \frac{n(\mathbf{r}')}{|\mathbf{r} - \mathbf{r}'|}\mathrm{d}\mathbf{r}' - V_{XC}(r). \tag{2.41}$$

More details of this generation scheme, including expressions for the total energy and its derivatives, can be found in Laasonen *et al.* [Laasonen 93].

Compared to the norm-conserving case, the difference lies in the presence of the overlap operator S, the wavefunction dependence on the coefficients D_{nm}, and the fact that the number of beta-projector functions β_n are typically twice as large. However, unlike in the norm-conserving case, the transferability of the ultrasoft pseudopotentials can be improved in a systematic way by increasing the number of reference energies used per angular momentum state.

In this thesis, this ultrasoft type of pseudopotential will be used throughout, unless otherwise stated. Further details on pseudopotential testing will be covered in chapter 3.

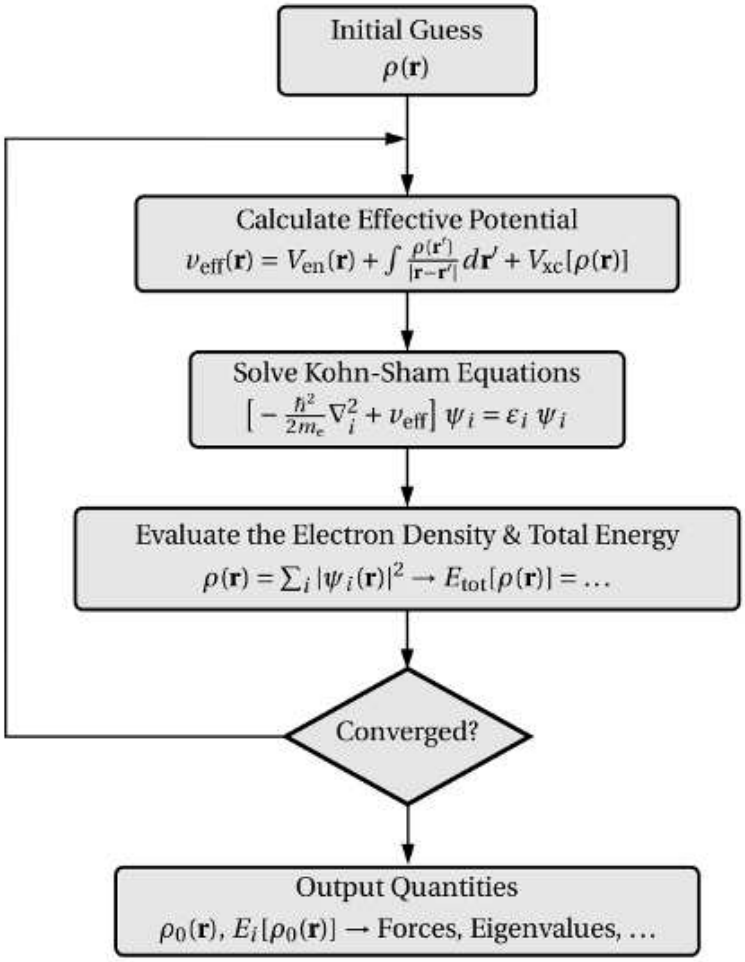

Figure 2.1: Flow chart for a basic electronic structure calculation.

2.5 Summary

To summarise, these are the basic steps of an electronic structure calculation, as illustrated in figure 2.5. It goes as follows:

1. Make an initial guess of the electron density $n(\mathbf{r})$.
2. Calculate the effective potential $V_{eff}(\mathbf{r})$.
3. Solve the Kohn-Sham equations for $\psi_i(\mathbf{r})$.
4. Evaluate the electron density $n(\mathbf{r})$ and the total energy $E[n(\mathbf{r})]$.
5. If converged, output quantities, if not, go back to step 2.

For more details on the basic theory and methods used in this thesis, see for example, Richard Martin's book on electronic structure [Martin 04]. Additionally, for details on designing effective calculations using these methods, see for example the review by Mattsson *et al.* [Mattsson 05].

Chapter 3

Pseudopotential Development

3.1 Introduction

Density functional theory calculation using plane waves and pseudopotentials (PWP-DFT) has been one of the fastest growing areas in science over the last 20 years. The success of the method, combined with the ready accessibility of user-friendly code, means that the technique is increasingly available to non-specialists. A typical ground-state PWP-DFT has several sources of error. Some of these are simply numerical and can be made negligible by more accurate computation: e.g. k-point sampling and completeness of the basis set. Some are more fundamental: the validity of the Kohn-Sham equations and, in particular, the accuracy of the semi-empirical exchange-correlation functional. In discussions of PWP-DFT results, discrepancies with experiment are typically associated with the failings of the exchange-correlation functional. A few percent error in lattice parameters, perhaps as much as 10% in elastic constants and point defect energies is typical. Most codes only treat a few bonding electrons quantum mechanically, the behaviour of the others being encapsulated in a description of an ion: the pseudopotential. There are many schemes for generating pseudopotentials, none of which are universally accepted.

Surprisingly few studies attempt to assign errors to the pseudopotentials. In fact, the majority of published work provides no detail about the pseudopotential used. This is despite the fact that all-electron calculations can be done for comparison in small systems, although basis set convergence can be hard to attain in practice for larger systems where forces are required. Even when comparisons of

pseudopotentials are made, they are normally non-systematic, between unrelated types of pseudopotential: "norm-conserving [Hamann 79, Kleinman 82] gives this, ultra-soft [Vanderbilt 90] gives that, PAW [Blöchl 94] gives the other". However, even for a given pseudopotential scheme, there is considerable variation between different parametrisations.

Titanium provides a good test case. Until recently there has been some controversy about which crystal structure is most stable. It is now widely accepted that calculations showing that the ω phase has the lowest structural energy are correct [Ahuja 93, Trinkle 03, Hennig 05]. The experimental observation of the *hcp* ground state then arises from contributions from zero-point energy and entropic effects. The ω phase is probably stable at low temperature, but cannot be easily formed as the transformation kinetics are slow.

In this chapter we present a detailed systematic study of the effects of parametrisation of pseudopotentials, showing that transferability errors are at least comparable with the errors normally associated with uncertainty in exchange-correlation. We also show how widely-used analysis techniques, such as projection onto local angular momentum states, can be dominated by the arbitrary choice of pseudopotential. We choose to study metallic titanium, because there are several competing crystal structures, *s*- *p*- and *d*-electrons are all present and, with only four valence electrons, explicit treatment of the $3s$ and $3p$ semicore states may be important.

3.2 Pseudopotential Generation

We generate our pseudopotential using the on-the-fly method implemented in the CASTEP code [Clark 05]. This method allows us to generate both norm-conserving and ultrasoft pseudopotentials, using the schemes by Lin *et al.* [Lin 93], and Laasonen *et al.* [Laasonen 93] respectively, as outlined in chapter 2.

For titanium it is natural to have at least three non-local angular momentum projectors representing s, p and d electrons. For wavefunctions with well-defined angular character, the results are insensitive to the details of the non-local beta-projectors.

As an example, a plot of the non-local beta-projectors and the local potential for a standard ultra-soft titanium pseudopotential is shown figure 3.1. Note that

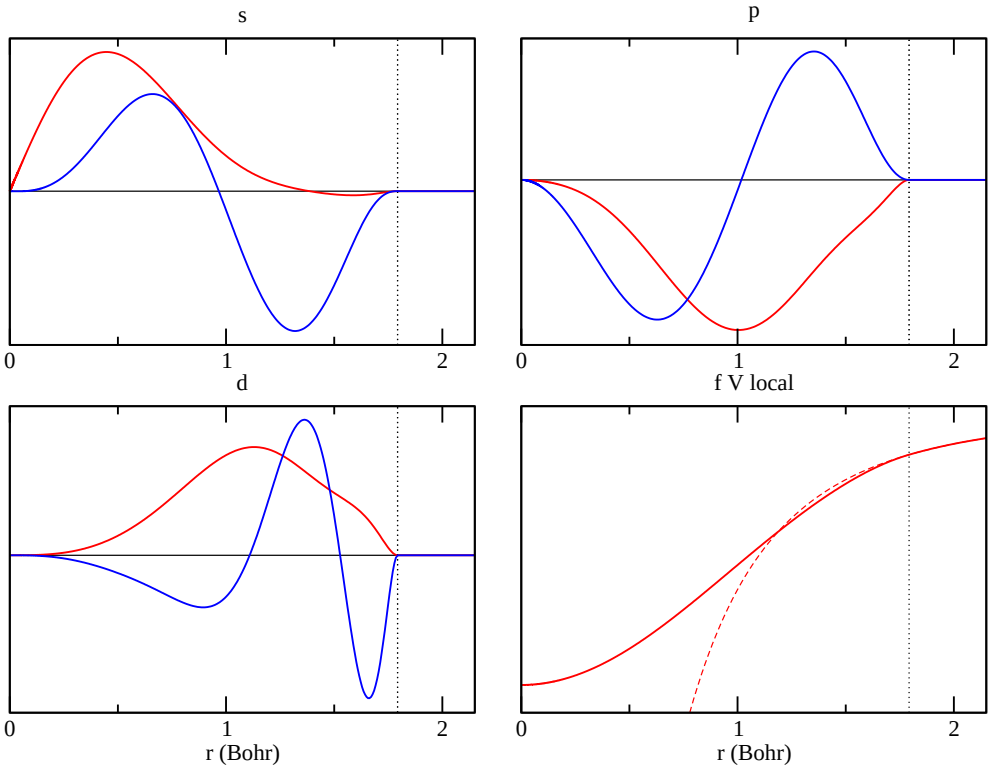

Figure 3.1: Beta-projector functions (s, p, d) and local potential (f) for a standard titanium pseudopotential, as generated by CASTEP, using the ultra-soft scheme described in chapter 2. The dotted vertical line is the cutoff radius r_{cl} for each reference state. Note that there are two beta-projectors for each angular momentum state, to improve the scattering properties. The dashed line in panel (f) is the reference all-electron potential V_{AE}, compared to the local potential V_{loc}. The atomic reference configuration used is $[3s^2 3p^6 3d^2 4s^2]$.

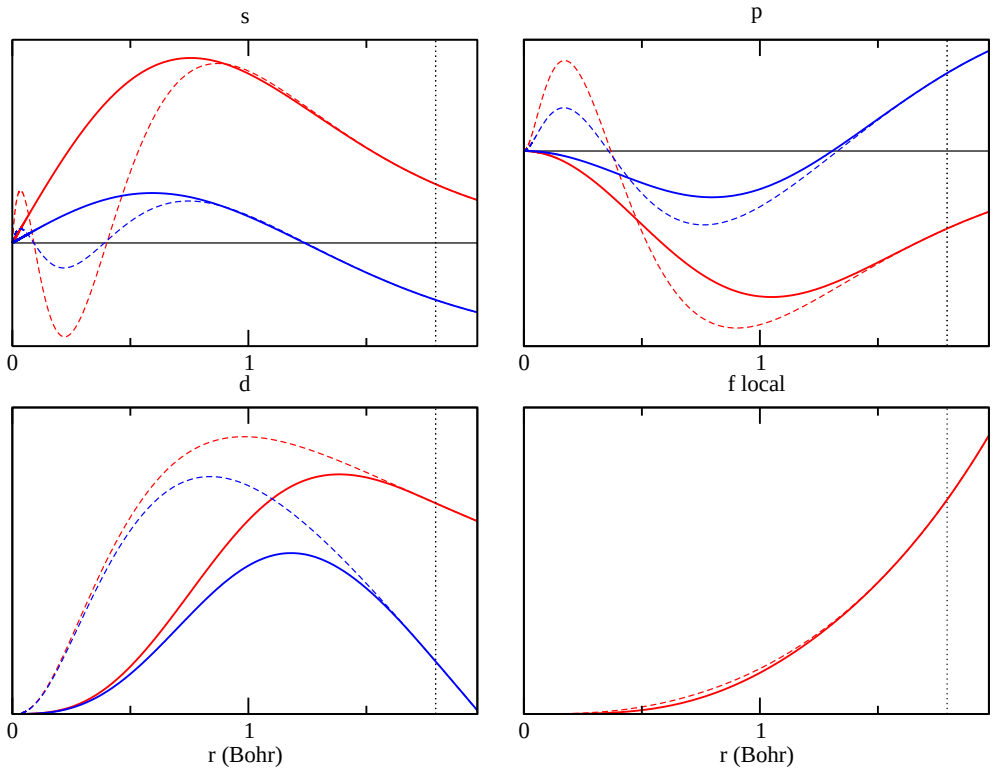

Figure 3.2: Partial pseudo- (solid lines) and all-electron (dashed lines) wavefunctions for a standard titanium pseudopotential, as generated by CASTEP, using the ultra-soft scheme described in chapter 2. The dotted vertical line is the cutoff radius r_{cl} for each reference state. Note the smooth, node-less appearance of the pseudo-wavefunctions inside the cutoff radius. The atomic reference configuration used is $[3s^2 3p^6 3d^2 4s^2]$.

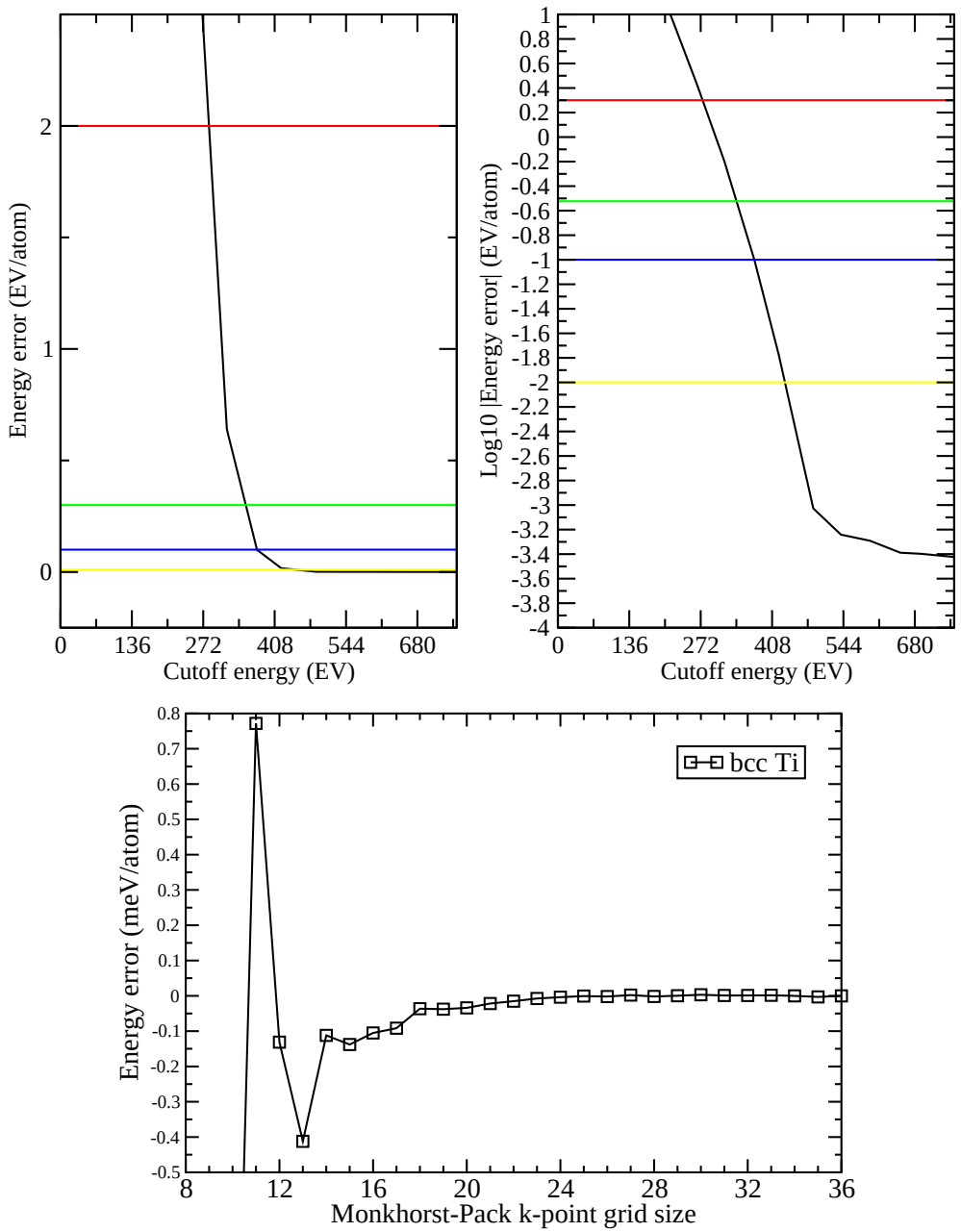

Figure 3.3: Energy convergence with respect to cutoff energy (upper panel) and Monkhorst-Pack k-point grid size (lower panel) for the standard titanium pseudopotential, as generated by CASTEP. The coloured lines indicate different levels of basis precision, ranging from coarse to extreme. Inspecting the upper plot, we find that a cutoff of 500 eV is reasonable for this pseudopotential. Moreover, inspecting the lower plot we find that the energy for the bcc phase converges using a grid size of $23 \times 23 \times 23$ k-points. The atomic reference configuration used is $[3s^2 3p^6 3d^2 4s^2]$.

there are multiple beta-projectors per angular momentum in this case, to improve the scattering properties of the pseudopotential.

Furthermore, a plot of the partial all-electron and pseudo-wavefunctions for the same titanium pseudopotential is shown in figure 3.2, showing the smooth, nodeless character of the pseudo-wavefunctions inside the cutoff radius.

Finally, the energy convergence with respect to the kinetic energy cutoff and k-point density for the same pseudopotential is shown in figure 3.3, which shows that the pseudopotential converges rapidly with cut-off about 470 eV, after which convergence is much slower. Furthermore, we find that the energy for bcc Ti converges well using a grid size of $23 \times 23 \times 23$ k-points.

There are then essentially five free parameters which can be varied in making the pseudopotential:

- The occupation of the *s*- , *p*- and *d*-levels in the atomic reference configuration.
- The choice of local channel.
- The cut-off radius at which the all-electron and pseudo-wavefunctions are matched.

The third is not truly free, since properties should converge as the radius is reduced, similarly the choice of local channel should have no effect if all the electrons are projected onto either *s*-, *p*- or *d*-orbitals. Thus the main degree of freedom is the atomic reference configuration.

In the case of titanium, one other issue merits consideration: whether to include the semi-core $3s$ and $3p$ electrons as valence. Conventional wisdom has it that these should be included. At first glance, this seems sensible, however it has two drawbacks: computationally, calculations with 12 electrons per atom are significantly slower than with 4; secondly, fitting the pseudopotential to $3s$ and $3p$ orbitals may compromise the accuracy of the fit to $4s$ and $4p$, which are the states responsible for the metallic bonding.

There is a self-consistent way to choose the atomic reference configuration: one can choose a reference solid crystal structure (e.g. *hcp* titanium at zero pressure) and choose the occupation of atomic s, p, and d levels which matches that found in the beta-projectors of the atom. As we shall see, in metallic Ti, the *spd* occupations are fairly insensitive to crystal structure.

In quantifying pseudopotential error, we will compare only "good" pseudopotentials. "Good" is a subjective criterion: here we constrain our definition of "good" to a series of tests on the atomic all-electron and pseudo-wavefunctions, namely:

- Reproduce the AE eigenvalues for the valence states.
- Give smooth pseudo-wavefunctions without nodes.

In order to fulfil the second criterion, we use a mixed ultrasoft-norm-conserving scheme for our 4-electron pseudopotentials, which avoids nodes on pseudisation, without becoming excessively hard [Bachelet 82], tested using the scheme by Troullier and Martins [Troullier 91].

In comparing multiple pseudopotentials, it is also useful to have some reference to compare with: here we choose two, the widely-used standard from the CASTEP library, and earlier results on norm-conserving potentials by Trinité *et al.* [Trinité 08].

3.3 Pseudopotential Testing

We present our results to address specific questions, posed in the subsections below. Unless otherwise specified, the solid state calculations were carried out using CASTEP, using the PBE-GGA approximation of the exchange-correlation term [Perdew 96]. We use an energy cut-off of 350 eV for the 4-electron pseudopotentials and 500 eV for the 12-electron pseudopotentials, (as seen in Fig. 3.3). We use a $23 \times 23 \times 23$ Monkhorst-Pack grid [Monkhorst 76] for the k-space integration for all three phases.

3.3.1 Does the crystal structure depend on the pseudopotential?

The main result of this study is that the crystal stability depends on the pseudopotential. Figure 3.4 shows the energy differences $E_{bcc} - E_{hcp}$ (a) and $E_{omega} - E_{hcp}$ (b) as a function of $4p$-electrons in the reference state for pseudopotentials generated using two different schemes, either including or excluding the $3s$ and $3p$ electrons from the core, yielding either a 12-electron

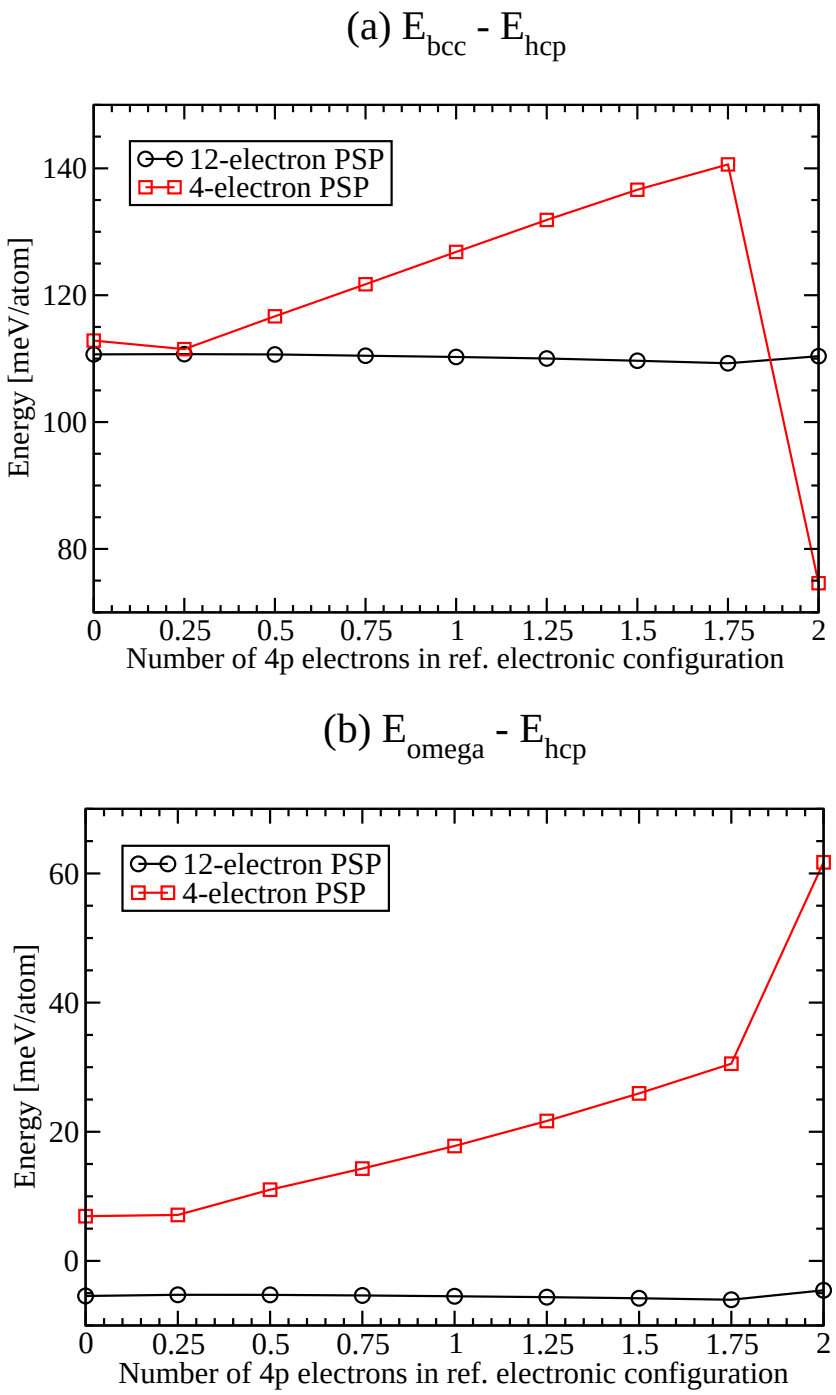

Figure 3.4: (a) $E_{bcc} - E_{hcp}$ in meV per atom as a function of the number of $4p$ electrons for two different pseudopotentials. (b) $E_{\omega} - E_{hcp}$ in meV per atom as a function of the number of $4p$ electrons for two different pseudopotentials. The anomalous data points on the right of both 4-electron PSP plots are due to the $3d$ states being empty, leading to unphysical results.

or a 4-electron pseudopotential. The striking difference is that the two kinds of pseudopotential give different results, where the 4-electron version stabilises the *hcp* compared to the *bcc* and the ω phase, whereas the 12-electron case does not, (as seen in fig. 3.4). The two anomolous points in figure 3.4 are due to the $3d$ states being empty, which leads to unphysical results. Moreover, our main results are in agreement with previous results by Trinité *et al.* [Trinité 08].

3.3.2 How do the atomic eigenvalues depend on the reference configuration?

Figure 3.5 shows the atomic eigenvalues for the all-electron atom and the pseudoatom as a function of the reference configuration. A good fit between these is regarded as a test of the pseudopotential. What happens here is that as one includes more $4p$ in the reference configuration, the core charge is less well screened. All eigenvalues are reduced, with the $3d$ being most affected, as one would expect given its more compact distribution. It is also notable that the error in the fitting methodology is much smaller than the uncertainty due to the reference configuration itself, arising from the environment in which the electron finds itself.

The consequence of this is that having more p-electrons in the reference configuration lowers the relative energy of d-electrons. One might expect this to give higher d-occupation in the solid, but comparing the *spd* projections in figure 3.6(a) with the atomic eigenvalues in figure 3.5 shows this is not so: as the d-electron in the atom becomes more stable, so the projected d-electron density in the solid is reduced. This apparent contradiction implies that the shift in atomic eigenvalue is due to different screening from the other electrons in the atom, rather than being a single particle effect. When the pseudoatom is placed in the different screening environment of the solid, the relative eigenstate mean energies are all shifted.

3.3.3 Do angular effects depend on crystal structures?

Figure 3.6 compares the number of electrons in each nonlocal angular momentum projection from relaxed configurations of *hcp*, *bcc* and ω. Two different pseudopotentials are shown. The figure shows that the occupation of each orbital

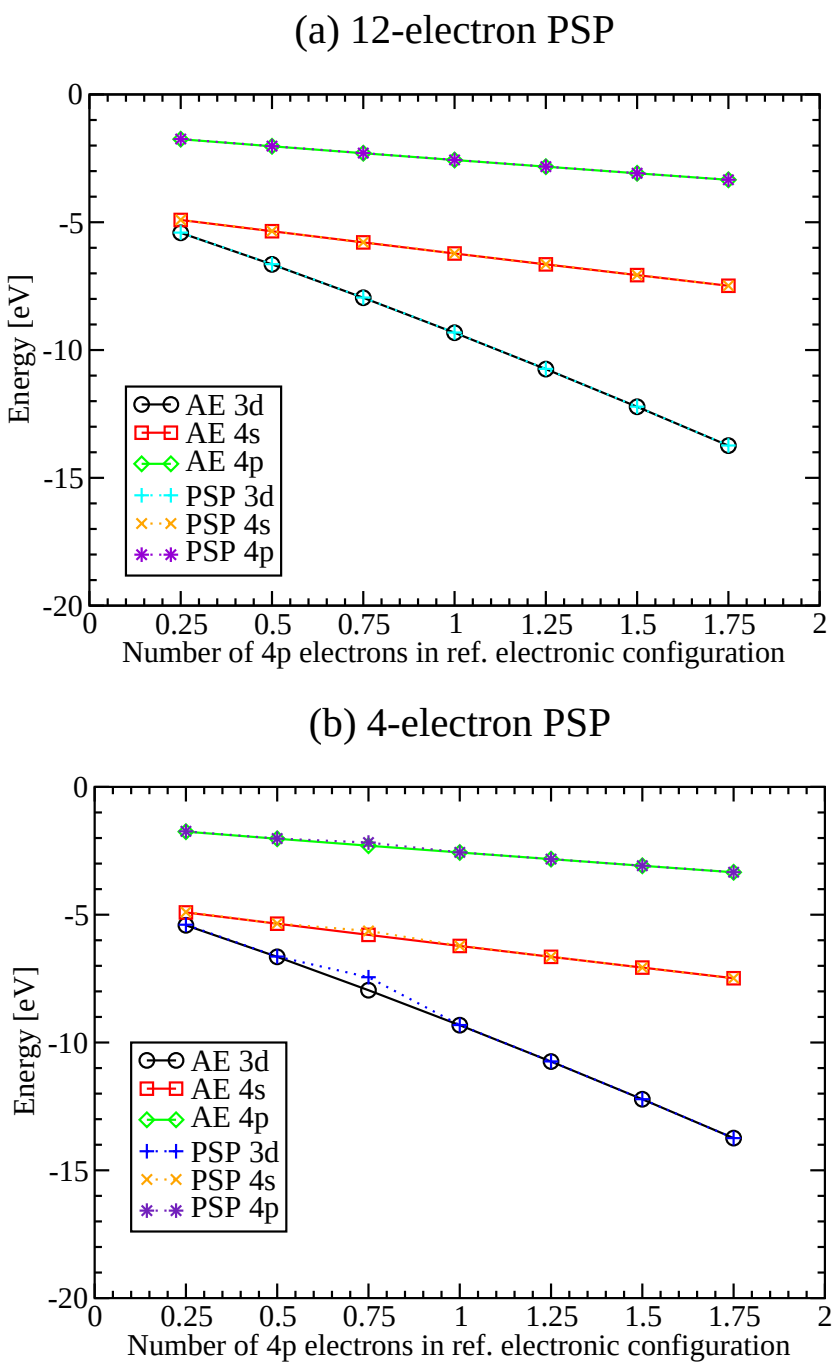

Figure 3.5: $3d$, $4s$ and $4p$ eigenvalues as a function of the electronic reference configuration. The AE values (open symbols with solid lines) are the all-electron eigenvalues, whereas the PSP values (crosses with dashed lines) are the matched pseudopotential eigenvalues. The figure shows that the pseudopotential faithfully reproduced the energies, and inspection of the wavefunctions (as in figure 3.2) shows no oddity. Thus we conclude that all these pseudopotentials are reasonable.

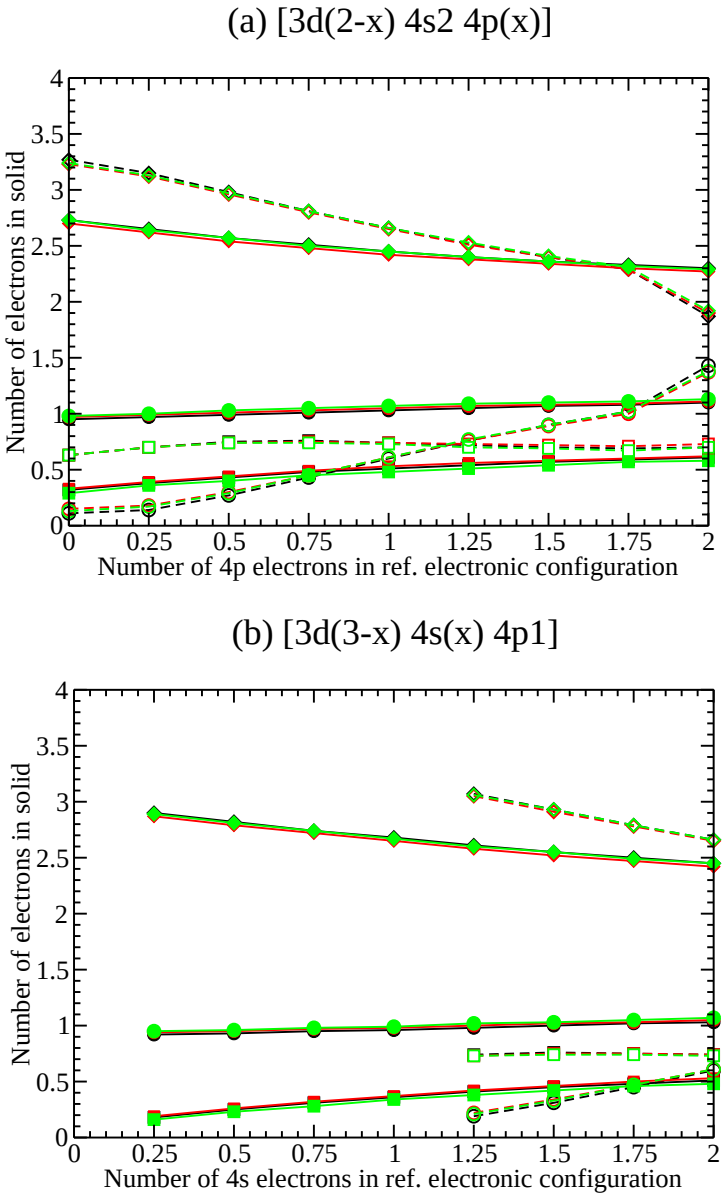

Figure 3.6: Number of electrons in the solid for each angular momentum state l. 4s-electrons are squares, 4p electrons are circles and 3d-electrons are diamonds. The open symbols shows 4-electron pseudopotentials with atomic configurations of (a) $[3d^{(2-x)}4s^24p^x]$ and (b) $[3d^{(3-x)}4s^x4p^1]$. The filled symbols shows 12-electron CASTEP pseudopotentials, with atomic configurations of (a) $[3s^23p^63d^{(2-x)}4s^24p^x]$ and (b) $[3s^23p^63d^{(3-x)}4s^x4p^1]$. The different crystal structures are represented by different colours, with *bcc* being black, *hcp* red and ω green. The graph shows that the projected number of electrons in each channel is independent of crystal structure, but strongly dependent on the pseudopotential: in most cases the three lines lie on top of one another.

Ref. configuration	$E_{bcc}^{tfr} - E_{hcp}^{tfr}$	$E_{\omega}^{tfr} - E_{hcp}^{tfr}$	$E_{bcc} - E_{hcp}$	$E_{\omega} - E_{hcp}$
$3s^2 3p^6 3d^1 4s^2 4p^1$	-104.22	-31.84	110.26	-5.47
$3d^1 4s^2 4p^1$	-67.75	-29.12	126.83	17.80

Table 3.1: Contribution from electron transfer to energy difference in meV per atom between structures for two different pseudopotentials.

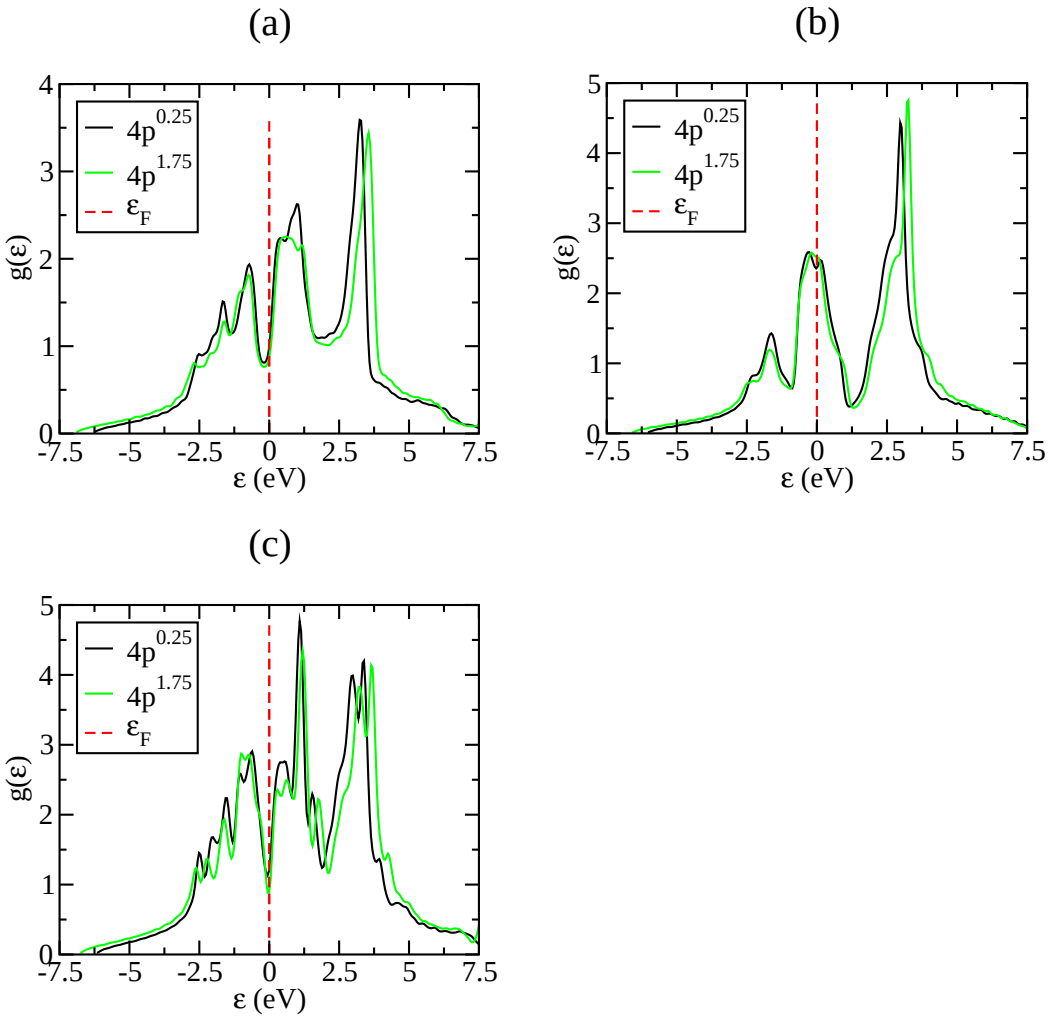

Figure 3.7: Densities of states for *hcp*-Ti (a), *bcc*-Ti (b), and ω-Ti (c), for two different 4-electron pseudopotentials with electronic configuration $[3d^{(2-x)}4s^2 4p^x]$. The dashed line represents the Fermi energy. The $4p^{1.75}$ configuration gives a broader *s*-band with the peaks being shifted slightly towards a higher energy due to having more *s*-electrons, (see figure 3.6).

depends strongly on the pseudopotential, as expected from the differences in atomic eigenvalues. However, the crystal structure has negligible effect on the relative occupations. This disproves the commonly-held idea that some structures are favoured by *d*-electrons, others by *s*-electrons on account of the bond angles present in the structure. To make this comparison qualitative we calculate, for each crystal structure, the energies of the atomic orbitals weighted by their occupation in the crystal. The contribution from electron transfer between states to the total energy difference between crystal structures can be written as:

$$E_c^{tfr} = \sum_l (n_l^c - n_l^{atom}) E_l^{atom} \tag{3.1}$$

where E_l^{atom} are the atomic eigenvalues of the l angular momentum state, and n_l^c, n_l^{atom} are the crystal and atomic occupation respectively. The relevant factor is the difference in this quantity between different crystal structures. Table 3.1 shows that although *spd* occupations differ by less than 0.01 between crystal structures, this term is significant compared to the total energy difference. However, in most cases it has the opposite sign, so cannot be regarded as the causal factor.

Figure 3.7 shows the densities of states around the Fermi level for two different 4-electron reference configurations $[3d^{(2-x)}4s^2 4p^x]$, with $x = 0.25$ (black) and $x = 1.75$ (green), for the three different crystal structures: *hcp* (3.7a), *bcc* (3.7b) and ω (3.7c). The different configurations cause a slight change in the density of states, with the $4p^{1.75}$ having a broader *s*-band with a higher number of *s*-electrons, (see figure 3.6), and the peaks above the Fermi level being shifted slightly towards a higher energy.

Thus we have shown that although the *spd*-occupation is strongly dependent on the pseudopotential, it is essentially independent of the crystal structure and plays no significant role in crystal structure stability.

3.3.4 How does the pseudopotential affect volumes?

Figure 3.8 shows the effect of the calculated solid volumes due to including various amounts of $4p$ electrons in the atomic reference configuration. The results show that even for norm-conserving pseudopotentials, apparently reasonable choices of pseudopotential can give variations in volume of a few percent, comparable to

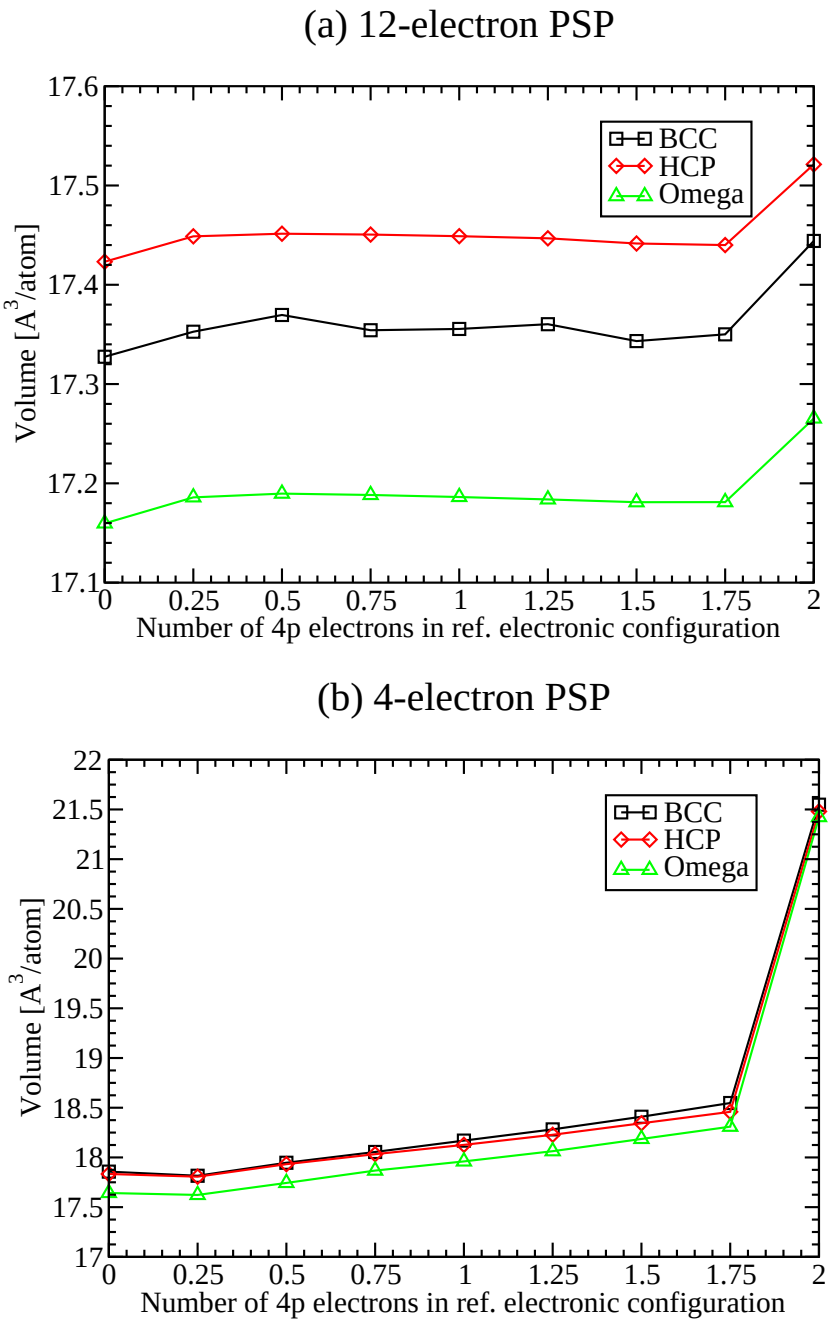

Figure 3.8: Volume change as a function of the electronic reference state of the atom. Pseudopotentials generated with atomic states lacking p or d electrons are anomalous, otherwise there is a strong variation in volume for the 4-electron pseudopotentials, but only weak variation for the 12-electron ones.

that due to different exchange-correlation functionals.

The $3d$ orbital is more compact than the $4s$ and $4p$, and as a consequence when there are more $3d$ electrons, the volume is smaller. Figure 3.6 showed the s-, p-, and d-orbital occupations for each crystal for each pseudopotential, which is consistent with this picture.

3.4 Discussion and Conclusions

We have shown that the effect of apparently arbitrary choices in the construction of the pseudopotential can strongly affect the results of atomic calculation, changing equilibrium volumes by up to 10% and changing the crystal structure. In the case of titanium, it is possible to associate some features of the solid with the choice of reference configuration.

The most striking result is that the stable crystal structure is pseudopotential dependent. At 0 K, all the 12-electron potentials have the ω phase as the most stable, while the 4-electron ones have *hcp*. For pseudopotentials generated with a $3d^1 4s^2 4p^1$ configuration, the calculated $hcp \rightarrow \omega$ transition pressures are -2 GPa and +17 GPa respectively. The corresponding *hcp* volumes per atom are 17.76 Å^3 and 16.24 Å^3 respectively. In part this is related to the overestimation of the volume by the 4-electron potentials: but since the experimental volume (17.55 Å^3 per atom, [Trinité 08]), requires an external pressure of about 5 GPa for the volumes to match, this does not account for the whole effect.

Furthermore, all-electron calculations on Ti give the ω phase as the most stable [Ahuja 93], which is in agreement with our 12-electron pseudopotential results, thus validating our approach as a sensible approximation.

The study also underlines some of the large errors associated with the pseudopotential method, and the impressive way that these errors cancel in some cases. For reasonable choices of reference state, the eigenvalues of the atomic reference state can vary by several tenths of an eV. These are faithfully reproduced by the pseudopotential, implying that the band structure isn't affected by the choice of reference state.

The results also cast serious doubt on the use of *spd*-projected densities of states for quantitative understanding, as these quantities are much more dependent on arbitrary choices in the pseudopotential than on the crystal

structure itself.

Chapter 4

Binary Titanium Alloys

4.1 Introduction

Titanium alloys are important for many applications, especially in the aerospace industry, where low density, high strength and corrosion resistance are paramount. Most commercial alloys contain secondary alloying elements such as V, Cr, Mo, Fe, Nb, Zr, La, Sn or Al.

After some years of controversy, it is now generally accepted that at zero temperature the ω phase of Ti has the lowest free energy [Ahuja 93, Rudin 04]. At finite temperature, vibrations and entropy play an important role. Under ambient conditions the α (hcp) phase becomes stable, and at high temperatures, (above 1150 K), the β phase (bcc) is stabilised by a combination of electronic and phonon entropy. This complicated behaviour is possible because the free energy of all three phases is very similar. Relatively small amounts of alloying elements alter these free energies, and can have a significant effect on the transformation temperature, perhaps eliminating it altogether [Trinkle 03, Hennig 05, Trinkle 06]. There are also significant alloying effects on high-pressure structures [Tegner 11]. The most common additives in Ti alloys are Al, which stabilises α, and V and Cr, which favour β. Additives also play additional roles in machinability, corrosion, and hardening; however the unanticipated side effects on phase stability can be problematic: For example, La was expected to improve machinability by lowering melting points of β alloys, but in fact forms brittle LaSn precipitates which actually hinder machining [Siemers 09].

Density functional theory (DFT) calculations provide a reliable technique

for calculating the Gibbs free energy, which determines the stability of crystal phases at ambient pressure. This is normally done by separately evaluating two contributions: H_0, the electronic ground-state enthalpy, and F_{vib}, a phonon contribution involving zero point energy, vibrational energy, and entropy.

A general rule appears to be that *sp* elements are α stabilisers while transition metals, even Zn and Cd which adopt the hcp structure, are β stabilisers. However, the strength of the stabilisation effect is unquantified. Here we apply DFT to show that the effects of alloying with different elements may be treated quantitatively as a function of *d*-band filling only. This provides a modern confirmation and specific application of ideas that date back to Hume-Rothery [Hume-Rothery 50, Pettifor 70, Pettifor 84, Pettifor 86, Pettifor 95].

4.2 Computational Method

The calculations are performed using CASTEP [Clark 05], a plane wave code with ultrasoft pseudopotentials [Vanderbilt 90] that we have thoroughly tested (see Chapter 3). The generalised gradient approximation of Perdew and Wang with the Perdew-Burke-Ernzerhof parametrization [Perdew 96] is used for the exchange-correlation energy. For chromium, scandium, titanium and vanadium, we treat the semicore $3s$ and $3p$ states as valence states, in addition to the usual $3d$ and $4s$ states. Supercell sizes of up to 24 atoms are used to get impurity levels down to 4 at.%. A plane-wave cutoff of 500 eV is used to ensure energy convergence. The *k*-point mesh density used for each configuration is 0.05/Å. For supercells containing more than one impurity atom, a number of different chemical decorations were tried, using a scheme similar to the special quasirandom structures (SQS) approach by Zunger et al. [Zunger 90]. For each crystal structure at a given alloying concentration, all possible configurations with the alloying atoms positioned at first, second, and third nearest neighbours were calculated. These configurations lead to representative error bars in Fig. 4.1 and multiple points in Fig. 4.5. The small scatter of these points shows that local ordering typically contributes only a few meV per atom, in agreement with other calculations on Ti_3Nb alloys [Lazar 11], although we note in passing that the local ordering does have a significant effect on the lattice parameter.

Elastic modulus calculations were carried out using finite stresses, with the

internal positions allowed to rerelax. Changes in energies and analytic stresses then give two semi-independent (and consistent) measures of bulk and shear moduli. We found that the bulk modulus is insensitive to either local order or composition, but the shear moduli, particularly in β alloys, vary greatly between compositions.

4.3 Results and Discussion

The relative stability of Ti-X (X = Al, Cr, Mo, Nb, Sc, V) alloys for a range of concentrations is shown in Fig. 4.1. The inset shows results when the atoms are constrained to their crystal lattice sites, while the main figure allows all atoms to be relaxed within the broken symmetry due to the added impurities. In cases where the bcc structure is not mechanically stable, this full relaxation gives an unrepresentatively low energy for bcc, leading to the large apparent scatter on the left hand part of the graph. The results show that the stabilisation effect is insensitive to the short-range atomistic order in the cell, and ternary data show that the stabilising effect is additive. Adding Sc, an α-stabiliser, [Savitskii 62, Liu 08] counters the effects of V and Cr in exact proportion to its effect in reducing the number of valence electrons. By contrast, the nontransition metal Al, although correctly found to be an α stabiliser, does not follow the linear relation. This observation leads us to propose that the effect of Sc, Nb, V, Cr and Mo comes from the same mechanism, the filling of the d band. Furthermore, these results agree well with previous theoretical results on low-modulus Ti-alloys, [Ikehata 04, Raabe 07, Hu 08] and with recent experimental results [Tane 10].

To test this hypothesis, the calculations were repeated by L. Zhu [Tegner 12] using the virtual crystal approximation (VCA) [Bellaiche 00] as implemented in CASTEP [Clark 05]. The disordered alloy is modelled as a unit cell comprised of mixture atoms defined by a pseudopotential that is generated as the weighted average of those for each atomic species. The same exchange correlation functional and other settings as in the supercell calculations above were used. The energy and stress tolerance for the cell relaxation is set to 5×10^{-5} eV and 2×10^{-2} eV/Å, respectively. The VCA has long been discarded as a method for reliable alloy calculations due to the inadequacy of relying on an "effective atom." For a metal, VCA produces the correct number of electrons per atom, but also

an "averaged" density of states, which introduces an error if the local density of states is very different on the two atom types. Our *d*-filling hypothesis requires that the density of states is similar on all atoms: just as the VCA presupposes. Thus, we regard the VCA calculations not as a reliable description of the material, but as a test of the *d*-band filling hypothesis. As can be seen in Fig. 4.1, despite the lack of atomic detail, the VCA tracks the changes in phase stability well.

The *d*-band hypothesis implies that the VCA will fail completely to describe the *p*-band additive Al. Sure enough, we find this to be the case relaxing to unphysical volumes even with the same 1s2s2p core: this may be understood as due to the *p*-band being full for the hybrid pseudo-ion, while it should not be for the Al ions.

A still-poorer approximation is to ignore alloying elements altogether and simply add electrons with a compensating background of positive charge. We use identical parameters as in the VCA calculations to investigate such "charged Ti" systems. Once again, Fig. 4.1 shows that the *d*-electron density alone stabilises the β phase, in a way exactly equivalent to that obtained with electrons associated with supercells and explicit atoms.

Additonally, we investigate the change in the c/a ratio of the α phase with changing composition as a proxy for hcp phase stability. Fig. 4.2 shows that the c/a ratio increases with increasing *d*-electron concentration, thus destabilising the α phase, which again is in agreement with our *d*-band hypothesis.

The notion that *d*-electron density is the crucial quantity is only reasonable if the electronic density of states (DOS) is roughly composition independent. DOS calculated with both VCA and supercell calculations are shown in Figure 4.3. It can be seen that they are indeed very similar in shape, the main effect of alloying is to move the Fermi level within the band. By contrast, the shape of the DOS for the Al-doped alloys is completely changed, once again showing that it is the *d*-electrons, not the ionic charge, which is critical. Thus we have shown that the enthalpy differences between the phases varies in proportion to the *d*-electron concentration. The Fermi level for each plot have been calculated using the cumultative densities of states, shown in figure 4.4.

To make the link to real materials for quantitative comparison, it is necessary to calculate the free energy. Zero-point and finite temperature contributions to the free energy (F_{vib}) can be obtained in several ways [Ackland 02, Baroni 01]. A

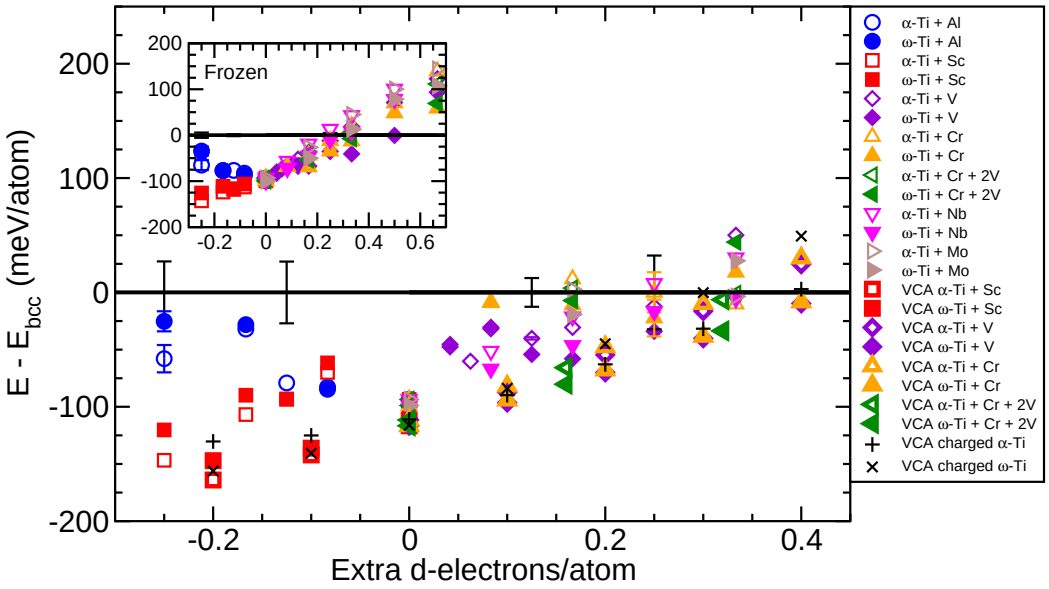

Figure 4.1: Phase stability of Ti-based alloys against number of valence electrons, calculated with the supercell method (normal symbols) and with VCA (bold symbols). Open symbols denote the hcp phase and filled symbols denote the ω phase. Bcc is the reference. Alloying elements are coded on a colour scale, with blue circles, Al; red squares, Sc; violet diamonds, V; orange up triangles, Cr; green left triangles, Cr+2V; magenta down triangles, Nb; brown right-triangles, Mo. Pluses are charged hcp and crosses are charged ω. Representative error bars show the difference in energy due to relaxation with the broken symmetry due to the added impurities and due to the different distribution of the impurities. The inset shows the results if the atoms are constrained to their lattice sites, and the error bars shows the energy difference simply due to different positioning of the impurities.

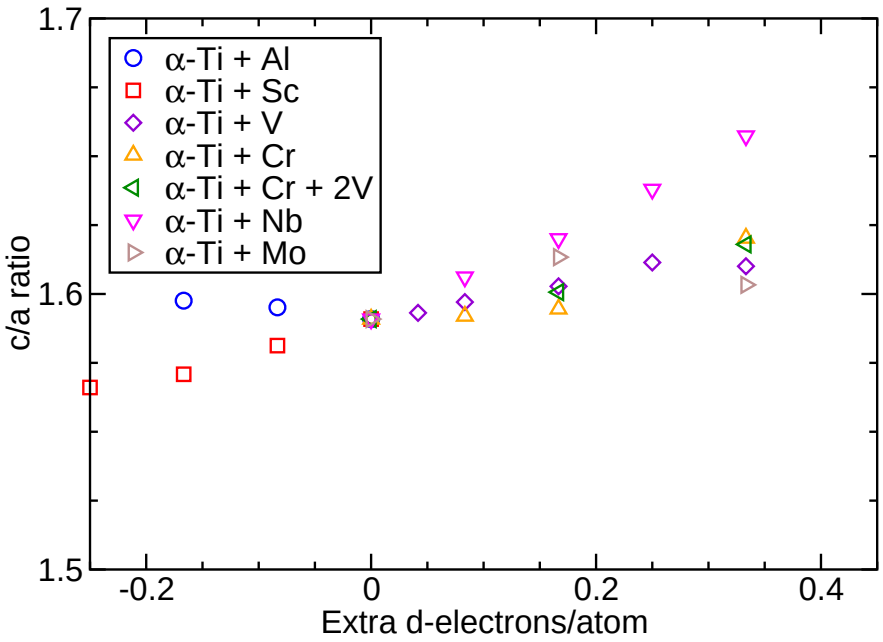

Figure 4.2: Change in c/a ratio for α phase Ti-alloys against number of valence electrons, calculated with the supercell method. Alloying elements are coded on a colour scale, as in Fig. 4.1, with blue circles, Al; red squares, Sc; violet diamonds, V; orange up triangles, Cr; green left triangles, Cr+2V; magenta down triangles, Nb; brown right-triangles, Mo.

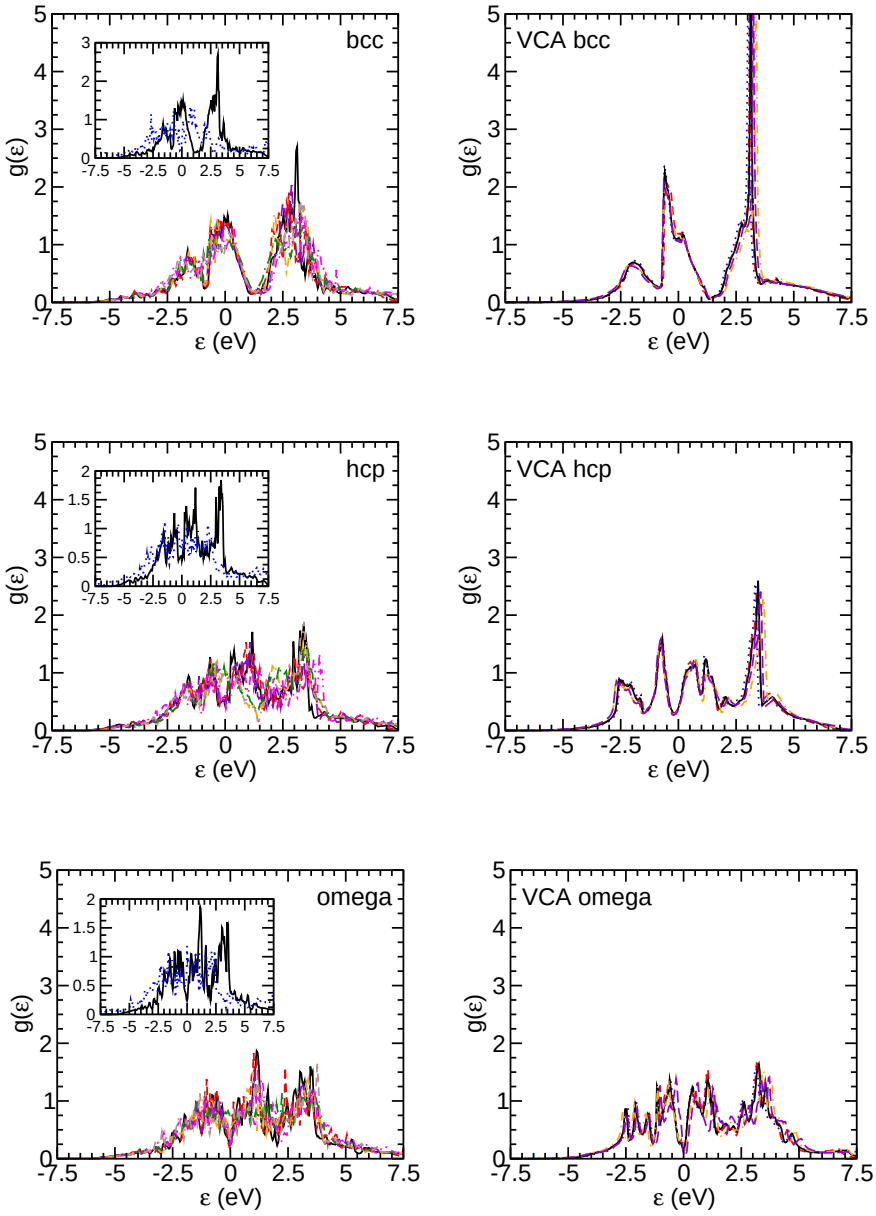

Figure 4.3: (Left) Densities of electronic states for alloys in the different phases, calculated with pure Ti (solid black line), Ti + 25% Sc (dashed red line), Ti + 33% V (long-dashed violet line), Ti + 33% Nb (dot-dot-dashed magenta line), Ti + 16% Cr (dot-dashed orange line), Ti + 16% Mo (dash-dash-dotted brown line) and Ti + 8% Cr + 16% V (dot-long-dashed green line). The inset shows the DOS for Ti + 16% Al (dotted blue line), compared with pure Ti. (Right) The corresponding plots for VCA, calculated with -0.2e charged Ti (dotted blue line), Ti + 20% Sc (dashed red line), pure Ti (solid black line), +0.4e charged Ti (dot-dashed orange line) and Ti + 40% V, (long-dashed violet line).

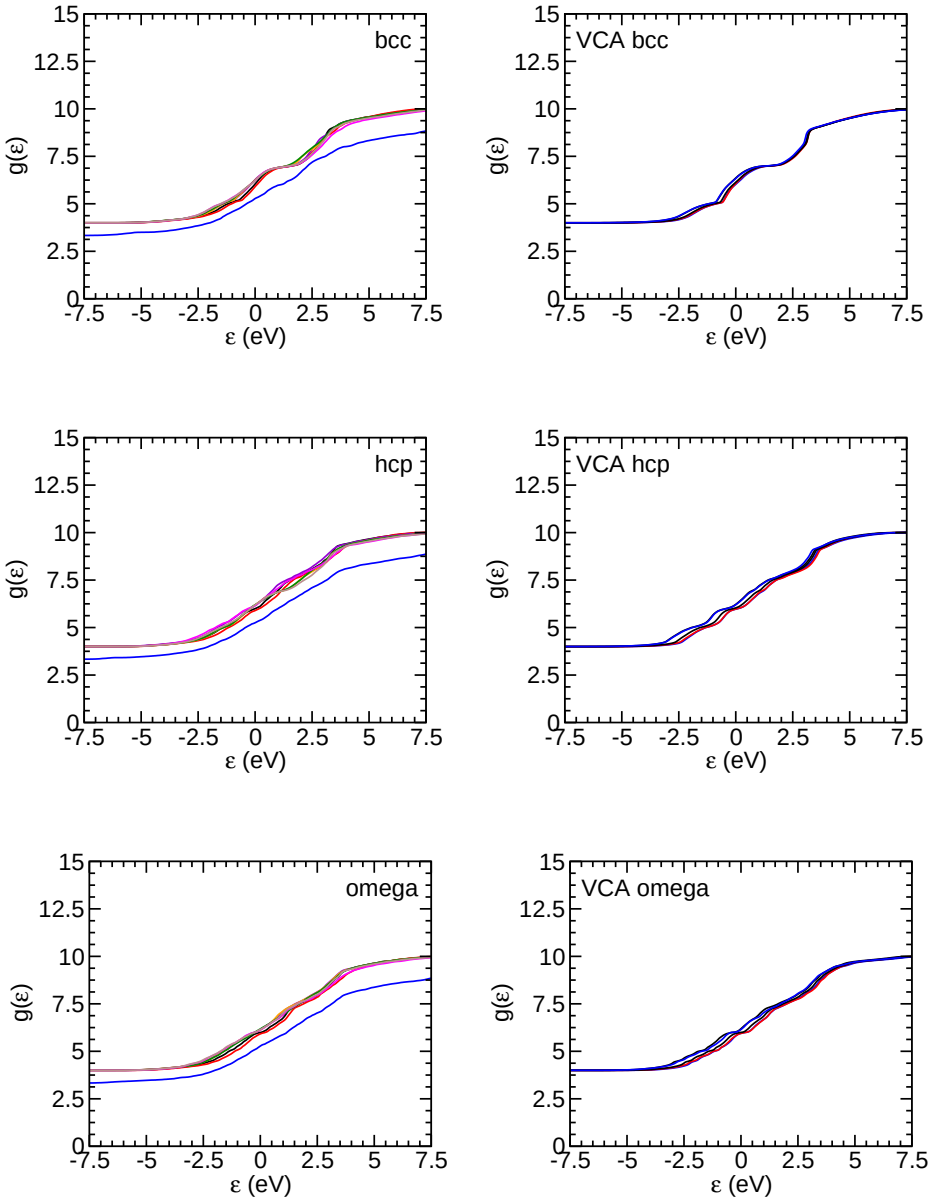

Figure 4.4: (Left) Cumulative densities of electronic states for alloys in the different phases, calculated with pure Ti (black line), Ti + 16% Al (blue line), Ti + 25% Sc (red line), Ti + 33% V (violet line), Ti + 33% Nb (magenta line), Ti + 16% Cr (orange line), Ti + 16% Mo (brown line) and Ti + 8% Cr + 16% V (green line). (Right) The corresponding plots for VCA, calculated with -0.2e charged Ti (blue line), Ti + 20% Sc (red line), pure Ti (black line), +0.4e charged Ti (orange line) and Ti + 40% V, (violet line).

full quasiharmonic phonon calculation fails for bcc-Ti, because this has imaginary phonon frequencies and is in any case computationally impractical for the large supercells used here. Although self-consistent phonon theory [Souvatzis 08]. has been shown to work for bcc-Ti, this is even more computationally demanding. A proven and practical method suitable for our purposes is to use the Debye approximation for the vibrational free energy [Moruzzi 88, Mei 09a]. The vibrational free energy per atom F_{vib} can then be expressed as

$$F_{vib}(\Theta_D, T) = \frac{9}{8} k_B \Theta_D - k_B T[D(\Theta_D/T) - 3\ln(1 - \mathrm{e}^{-\Theta_D/T})], \tag{4.1}$$

where $D(\Theta_D/T)$ is the Debye function.

Using the the approach by Chen and Sundman [Chen 01], we can determine the Debye temperature from

$$\Theta_D = s\frac{\hbar}{k_B}[6\pi^2 v^{1/2}]^{1/3} f(\sigma)\sqrt{\frac{B}{m}}, \tag{4.2}$$

where s is a geometric factor determined by the crystal structure, v is the volume per atom, B is the isotropic bulk modulus which can be easily calculated *ab initio* by finite strains of the supercells, m is the atomic mass and $f(\sigma)$ is given by

$$f(\sigma) = \left\{ 3\left[2\left(\frac{2(1+\sigma)}{3(1-2\sigma)} \right)^{3/2} + \left(\frac{(1+\sigma)}{3(1-\sigma)} \right)^{3/2} \right]^{-1} \right\}^{1/3}, \tag{4.3}$$

where σ is the Poisson ratio, which can be obtained from the elastic constants.

For pure Ti this gives $\Theta_D = 395$ K for the ω phase, $\Theta_D = 364$ K for the α phase [Mei 09a] and $\Theta_D = 276$ K for the β phase [Chen 01]. This is in good agreeent with previous work and shows the correct ω-α-β sequence with increasing temperature.

Using these results, we evaluate the phase transition temperatures for each composition. From this, we can construct phase diagrams for each binary and ternary system, and we find these to be in good agreement with experiment where available. However, to illustrate our central concept that structure depends on the *d*-electrons, we plot a combined phase diagram with *d*-electron number involving all Cr (+2), V (+1) and Sc (-1) alloys (Fig. 4.5). Remarkably, the phase boundaries for the individual systems are coincident when scaled in this

Table 4.1: Elastic constants (GPa) of bcc Ti-X alloys, calculated by L. Zhu using VCA, reprinted from [Tegner 12].

Extra *d*-electrons	-0.2	-0.1	0	0.1		0.2			0.3		0.4	
X	Sc	Sc	Ti	V	Cr	V	Cr	V-Cr	V	Cr	V	Cr
C_{11}	60	79	90	107	101	119	115	117	132	137	154	159
C_{12}	109	108	112	119	120	127	126	128	133	130	134	132
C_{44}	46	45	41	41	33	48	39	45	51	46	51	50

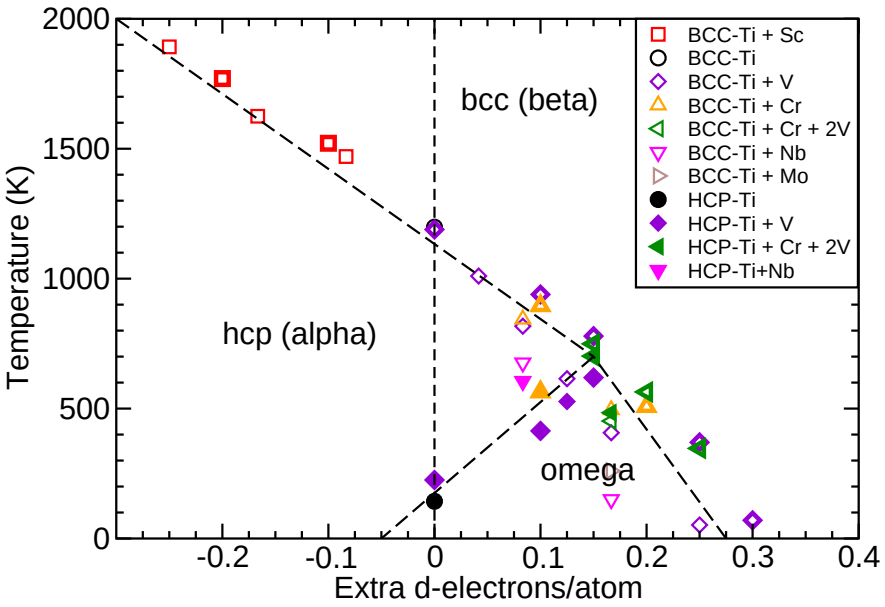

Figure 4.5: Phase diagram showing temperature against composition plotted as the number of valence electrons. Points show transition temperatures calculated with the supercell method (normal symbols) and with VCA (bold symbols). Alloying elements are coded on a colour scale as in Fig. 4.1. Approximate phase boundary lines are guides for the eye. The vertical dashed line is pure Ti, the reference. Binary diagrams can be deduced from this figure by considering only the data concerning a single alloying element, and rescaling the x axis according to its valence.

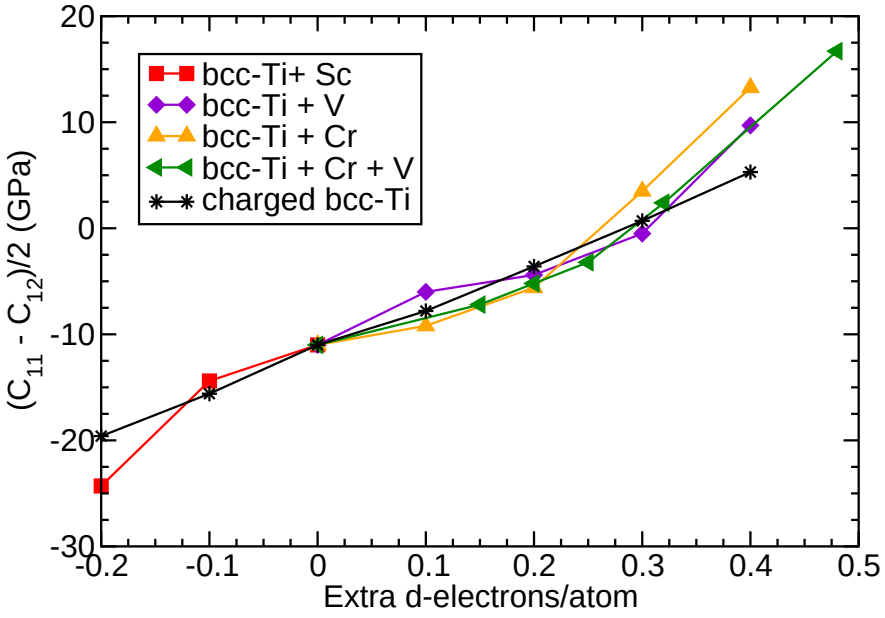

Figure 4.6: Elastic stability of bcc Ti-based alloys against number of valence electrons, calculated using VCA. The straight black line, fitted from VCA data obtained by simply adding extra electrons to a Ti unit cell, gives $C' = -11.6 + 42\Delta n_d$.

way, a data collapse that provides strong support for our theory.

Furthermore, we investigate the bcc-stabilising behaviour of the Cr ($\Delta n_d = +2$), V ($\Delta n_d = +1$) and Sc ($\Delta n_d = -1$) alloys by computing the zero temperature elastic constands C_{ij} and the shear constant $C' = (C_{11} - C_{12})/2$ versus number of d-electrons, using VCA. C' is known to be negative for pure Ti, and tuned close to zero for Ti-based Gum metal [Li 07] reflecting the mechanical instability of the structure. The results are shown in Table 4.1 and Fig. 4.6, showing that the variation in C' is also accounted for by the number of d-electrons alone. Once again, the even simpler charged Ti-system is included for comparison, and even this follows the same pattern. Although C' varies with temperature, this contribution is only weakly dependent on composition, so the near-linear relation should hold at all T.

Finally, we turn to the underlying cause of the unstable bcc structure. As can be seen in Fig. 4.3, the Fermi level in pure bcc-Ti is coincident with a peak in the density of states for Ti. This is an unstable situation, wherein a Peierls-type lattice distortion can split the peak and lower the enthalpy. As more electrons are added to the d band, through V and Cr alloying, the Fermi energy moves away from the peak. Although here we are only calculating properties of Ti alloys, this picture has much in common with that obtained for canonical d bands [Andersen 77]. The unstable mode is the T1N phonon which, coupled with a lattice distortion, is the established pathway for the bcc-hcp transition [Petry 91].

We have shown the alloying effects to be additive in multicomponent homogeneous material systems, however we recall that in many ternary and higher mixtures aging will cause phase separation with different compositions in the phases.

4.4 Conclusions

In conclusion, we are considering alloys produced by quenching, and therefore unable to phase-separate to the thermodynamic equilibrium. We find that chromium and vanadium stabilise the β phase, while scandium destabilises it. The strength of the effect is directly proportional to the additional d-electrons present in the alloying element. The effect appears to be additive, and the positional effects of the impurities appear to be small.

In the case of aluminium, our calculations show that it stabilises the α phase, rather than the β phase, but the simple d-electron sum rule does not seem to apply to this *sp* element.

While the correct stabilisation predictions of pseudo-potential calculations are unsurprising, we have also tested our hypothesis by comparing it with VCA and extra-electron calculations, which correctly capture the aspects of the physics we think are important. The accurate results obtained from these normally unreliable methods give strong support to the d-electron picture.

This puts the empirically known effects of α and β stabilisation on a firm theoretical footing. It also enables alloy designers to anticipate the phase-stabilising effects of additions which may be added for other purposes. Finally, it emphasises the need for the d-electron concentration to be considered as a parameter in any multiscale modelling approach.

Chapter 5

High-Pressure Studies of Ti-6Al-4V

5.1 Introduction

The titanium alloy Ti6Al-4V (Ti64) is the workhorse of the titanium industry, constituting of over 50% of total production [Boyer 96]. It is a two-phase alloy consisting of 6 wt.% aluminium, 4 wt.% vanadium, and the remainder titanium. It mainly crystallises in an Al-enriched α phase, with a much smaller fraction (around 10%) crystallising in a V-enriched β phase around the grain boundaries [Hayes 95]. Al acts as the main alpha-stabiliser and solid solution strengthener whereas V acts as a beta stabiliser and allows the alloy to be heat treated without grain growth and also improves weldability.

Despite the widespread industrial use of this alloy [Peters 03, Collings 84], remarkably little is known about its behaviour under extreme conditions such as high pressure [Chesnut 07, Halevy 10, Rosenberg 81, Gray 93]. This is in sharp contrast to pure titanium, which has been studied extensively, both computationally and experimentally. Most calculations predict pure Ti to undergo the following sequence of phase transitions with increasing pressure; $\alpha \rightarrow \omega \rightarrow \gamma \rightarrow \delta \rightarrow \beta$ [Joshi 02, Kutepov 03, Verma 07, Hao 08, Mei 09b, Hu 10]. The $\omega \rightarrow \gamma$ transition pressure is predicted to be 102–110 GPa [Verma 07, Mei 09b, Hu 10]. However, Joshi *et al.* [Joshi 02] and Ahuja *et al.* [Ahuja 04] calculated the transition from the ω to the β phase to take place at the lower pressure of 93 GPa [Joshi 02] and 80 GPa [Ahuja 04], with no intermediate phases. In most

cases the orthorhombic δ phase is calculated to be either energetically unstable, or to be formed as a consequence of the non-hydrostatic conditions present in the high pressure experiments [Joshi 02, Kutepov 03, Verma 07, Mei 09b]. The $\delta \rightarrow \beta$ transformation is predicted to occur below 200 GPa, at 161 GPa [Hao 08] and 136 GPa [Kutepov 03].

Moreover, DFT calculations have also revealed the reconstructive mechanism behind the martensitic $\alpha \rightarrow \omega$ transformation in Ti [Trinkle 03, Trinkle 05, Hennig 08] and also the effect that impurities such as oxygen have on the transition pressure [Hennig 05]. In fact, Hennig *et al.* [Hennig 05] predict the combined effect of the substitutional impurity Al (10.7 at.%) and interstitial impurity oxygen (0.5 at.%), is to suppress the $\alpha \rightarrow \omega$ transformation in Ti64 to 63 GPa.

Our motivation for conducting the present study was to determine the role of alloying in changing the phase behaviour of Ti alloys, specifically whether Ti64 exhibits similar behaviour to that reported for pure Ti at multi-megabar pressures in transforming to the γ and δ phases, and whether there is a direct $\omega \rightarrow \beta$ transition in the alloy. Moreover, MacLeod *et al.* [MacLeod 12] have made x-ray diffraction studies of Ti64 in a range of different pressure transmitting media (PTMs) to above 200 GPa, which we will describe and use in comparison with our electronic structure calculations. We have also investigated the effects of local ordering in Ti64 by comparing the observed structural behaviour with that calculated for structures with different ordering schemes.

5.2 Computational Details and Results

In order to obtain accurate information about the electronic and atomic structures of Ti64 we have conducted extensive electronic structure calculations. These allowed us to understand the physical basis for the different phase transition sequence observed in Ti64 compared to Ti, and to investigate the effects of the local atomic ordering within the alloy.

The calculations were conducted using the plane-wave DFT-code CASTEP [Clark 05], using supercells of 54 atoms for each phase, to get impurity levels of 2 at.%. The k-point grid density for each calculation was 0.05 Å^{-1}. A plane-wave cut-off of 500 eV was used for basis-set convergence. A generalised gradient

approximation [Perdew 96] was used for the exchange-correlation. In all cases, the alloy composition was 85.2 at.% Ti, 11.1 at.% Al and 3.7 at.% V, that is, 46 atoms of Ti, 6 atoms of Al and 2 atoms of V.

The theoretical thermodynamic ground state, at ambient temperature and zero pressure, is a three-phase mixture of hcp-Ti, bcc-V and Ti_3Al, an ordered, hcp-based DO19 intermetallic structure. As pressure increases only the Ti-rich phase is predicted to undergo transitions. Since most commercial Ti64 alloys have not undergone this full phase decomposition, we have assumed a single phase in the calculations.

Initially, we calculated a full set of chemical decorations for each crystal structure, following the same special quasirandom structure (SQS) [Zunger 90] approach (described in chapter 4) for the binary compositions $Ti_{48}Al_6$ and $Ti_{52}V_2$ which provide a best-possible sampling of the local arrangements of the impurity atoms. In all cases calculations were carried out at constant pressure and the atoms were allowed to relax from their ideal lattice sites. Normally the crystal structure was preserved, but in a few cases the relaxation took the sample through the hcp-bcc transition to the more stable phase (often twinned). Such cases are easily identified and were removed from the statistics.

Analysing the calculated energies from these data showed that there was a weak tendency towards a local ordering where the minor component atoms were located as far apart as possible. At ambient pressure this effect is negligible, (see chapter 4), but at higher pressure it becomes significant, of order 30 meV per impurity atom, with local ordering most strongly favouring the ω phase. The primary driving force for this local ordering appears to be the oversized Al atoms. SQS samples with Al on adjacent sites have larger volumes than those with separated Als, and are consequently disfavoured by high pressure.

There are several million (54!/48!/6!) permutations of the atoms in the $Ti_{46}Al_6V_2$, and even the ternary alloy SQS reduction leaves an unreasonable number to calculate. So we created two samples, one set of configurations with strong local ordering (avoiding impurity near-neighbours) and another set without any ordering tendency. The comparison between these sets with the calculated enthalpies of the ω and β phases, relative to that of the α phase, (at T = 0 K) as a function of pressure are shown in Figure 5.1. It can be seen that the calculated transition pressures are distinctly different depending on whether local ordering

is included. As we shall see, for the locally-ordered samples the calculated $\alpha \rightarrow \omega$ transition pressure is 24 GPa, in good agreement with the experimental results by MacLeod *et al.* [MacLeod 12] detailed in the following section. The transition pressure to the β phase is predicted to be around 105 GPa, again in good agreement with the experimental data by MacLeod *et al.* [MacLeod 12]. By contrast, if local order is excluded, then the calculations suggest that the ω phase will not be formed at all.

The calculated c/a ratio for the ω phase, assuming local ordering, is shown along with experimentally-observed values by MacLeod *et al.* [MacLeod 12] in Figure 5.5. The agreement both in terms of the absolute value of the ratio, as well as the pressure dependence, is reasonable. The most striking feature of this figure is the constancy of c/a over the pressure range, at precisely the value which brings the (110) and (101) diffraction peaks into coincidence. There is no symmetry equivalence between these peaks, and we attribute this locking effect to a Fermi Surface/Brillouin Zone interaction, consistent with the Hume-Rothery rules for its appearance in several materials with the same electrons/atom ratio [Hume-Rothery 34].

Above 60 GPa, we carried out calculations on pure Ti of the orthorhombic γ and δ phases [Vohra 01, Akahama 01], as well as the usual ω and β phases. These orthorhombic phases are subtle distortions away from hcp and bcc respectively, and we successfully reproduced previous calculated results from Verma *et al.* [Verma 07]. The energy and enthalpy curves are shown in figure 5.2. The δ phase is found to be energetically unstable, relaxing to the β phase, which leads to the strange jump in internal energy and causing the enthalpy curve to merge with bcc. The fact that the other energy curves do not cross can be seen as an indication that the phase transition is mainly driven by a volume change rather than energetics.

We then repeated these calculations on a few representative supercells of Ti64, starting with the atoms on positions corresponding to ideal γ and δ Ti. In all cases the atoms relaxed back towards the bcc positions. With the impurities already breaking the cubic symmetry, it is impossible to determine definitively in the calculation whether the orthorhombic distortion is absent. However, for the alloy, in all cases, we find relaxation to structures indistinguishable from those obtained starting from the cubic β phase. This is in agreement with the

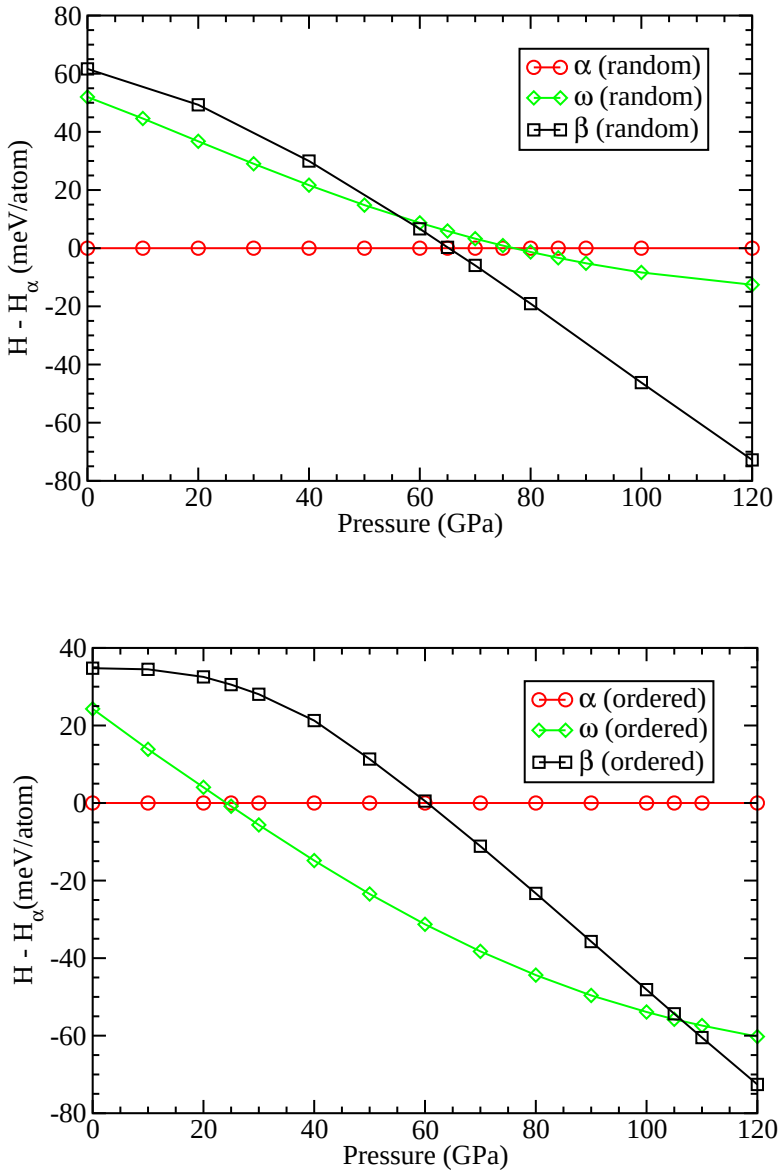

Figure 5.1: The calculated enthalpy differences between the ω and β phases, relative to that of the α phase, as a function of increasing pressure. The transition pressures are taken from where the lower curves cross. The upper graph shows the predicted transition pressures if the alloying atoms are ordered randomly, whereas the lower graph shows the transition pressures if the locations of the alloying atoms are locally-ordered so as to be distributed as far apart as possible.

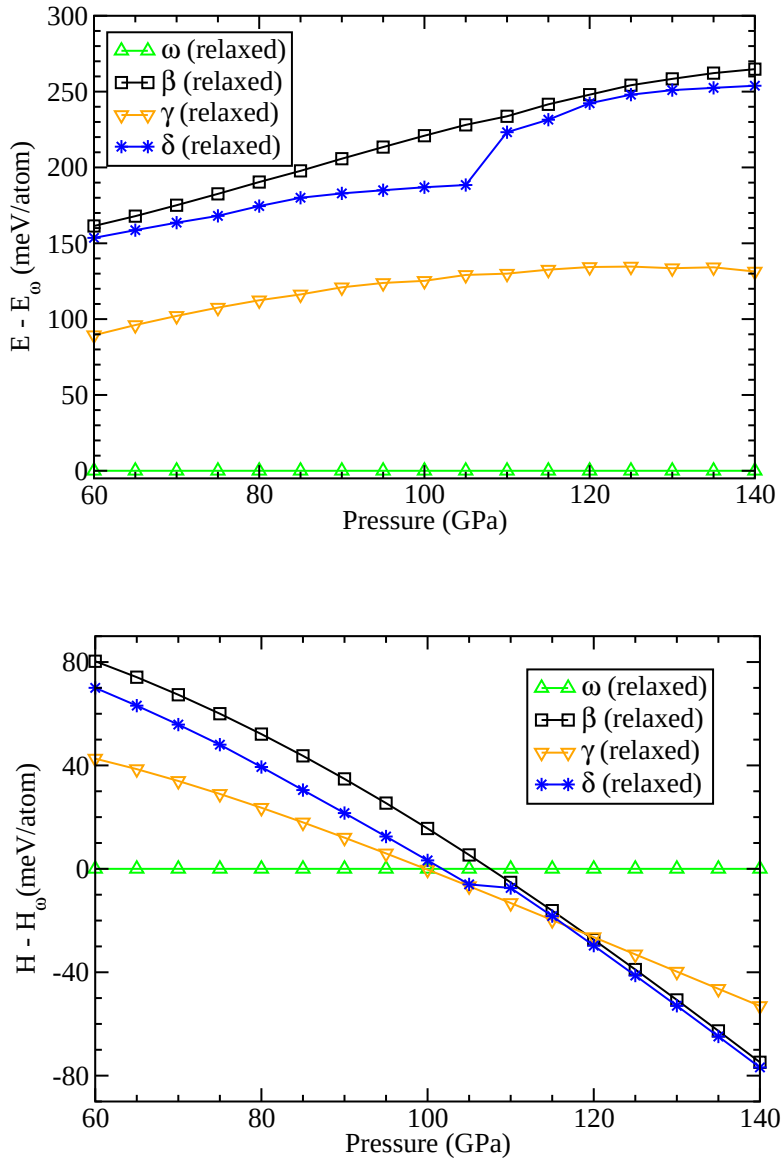

Figure 5.2: The calculated internal energy and enthalpy differences of pure Ti, relative to that of the ω phase, as a function of increasing pressure. The transition pressures are taken from where the enthalpy curves cross. The upper graph shows the internal energy change $\Delta U = \Delta H + p\Delta V$, indicating that the phase transition is driven by the change in volume rather than internal energy.

experimental observation by MacLeod *et al.* [MacLeod 12] of the γ and δ phases being absent for Ti64.

5.3 Experimental Details

Our collaborators MacLeod *et al.* [MacLeod 12] obtained powdered samples of polycrystalline Ti64, (commercially sourced from Goodfellow Metals), possessing an oxygen impurity level of 0.123 wt.%. These powders were prepared using plasma atomisation, a patented approach used by Goodfellow. In this, a wire is passed through three converging plasma torch jets, with the molten droplets of metal separating from the wire and cooling in a jacketed, inert column. The rapid cooling suggests that the local ordering will be frozen in from high temperature, and there will be insufficient time for nucleation of secondary, ordered, phases.

The samples were loaded into several membrane-driven diamond anvil cells, using a number of different pressure transmitting media (PTMs), to investigate the effects of non-hydrostaticity on the phase transition behaviour. In order of increasing hydrostaticity, the PTMs were: no PTM, mineral oil, 4:1 methanol-ethanol, and neon. Furthermore, Cu powder was used as the pressure calibrant [Dewaele 04] in all experiments except for that in which Ti64 was embedded in neon, as the neon PTM could also act as the pressure marker in that case [Dewaele 08].

Angle dispersive X-ray (ADX) powder-diffraction data were then collected at room temperature on the HPCAT (High Pressure Collaborative Access Team) beamlines 16-ID-B and 16-BM-D, at the Advanced Photon Source, Argonne National Labs.

For further experimental details, see [MacLeod 12].

5.4 Experimental Results

At ambient conditions, only diffraction peaks from the α phase were observed by MacLeod and coworkers. On compression, the α phase of Ti64 was then found to transform into the ω phase at slightly different pressures, (26.2 – 32.7 GPa), which may be related to the degree of hydrostaticity of the pressure transmitting medium. The experimentally observed phase transition pressures by MacLeod

et al. [MacLeod 12] for the $\alpha \rightarrow \omega$ phase transition in Ti64 are summarised in Table 5.1, together with previous measurements. The transition pressure for Ti64 embedded in a methanol-ethanol PTM is slightly higher than that obtained by Chesnut *et al.* [Chesnut 07] using the same PTM, and the α phase bulk modulus, $K_0 = 151(4)$ GPa, is in agreement with the Halevy result ($K_0 = 154(11)$ GPa). That said, the $\alpha \rightarrow \omega$ transition pressures are in good agreement with our calculated values.

However, the observed values for the $\alpha \rightarrow \omega$ transition pressure in Ti64 differ less than those observed for the same transition in pure Ti using different PTMs [Errandonea 05], and this similarity, and potential small variations in the experimental setup, seems to make any a link between the transition pressure and the hydrostaticity of the pressure environment difficult to quantify.

Moreover, the α and ω phases coexist over a pressure range of $\sim$10 GPa. Similar behaviour was observed in all of the experiments, and MacLeod *et al.* did not observe a large variation in the coexistence region depending on the PTM used. This behaviour is different to that reported by Errandonea *et al.* [Errandonea 05] in their study of the $\alpha \rightarrow \omega$ transformation in Ti.

Figure 5.3 shows the integrated ADX diffraction patterns collected by MacLeod *et al.* [MacLeod 12] from Ti64 embedded in a neon PTM as it was compressed into the ω phase. The onset of the transition in this sample was observed at 32.7 GPa, with the appearance of the dominant (110/101) diffraction peak at $2\theta \sim 10°$. In a second sample (also loaded in a neon PTM), the onset of the transition was observed at a pressure of 32.5 GPa. As the pressure was increased further, the (110/101) peak increased in intensity and other ω phase peaks such as (001), (201), (210), and others not shown in Figure 5.3, began to emerge until, at $\sim$45 GPa, the transformation was complete. Again, the observed transition pressures are in good agreement with our calculations.

In all but one of the Ti64 samples loaded in a methanol-ethanol PTM, failure of the diamonds occurred at the maximum pressures reached. Measurements on pressure decrease back to ambient pressure (actually 0.8 GPa) were thus only possible in this one sample. On pressure decrease from the ω phase, Ti64 were observed by MacLeod *et al.* [MacLeod 12] to transform completely back to the α phase, in contrast to Errandonea *et al.* [Errandonea 05] who recovered the ω phase for pure Ti loaded into methanol-ethanol.

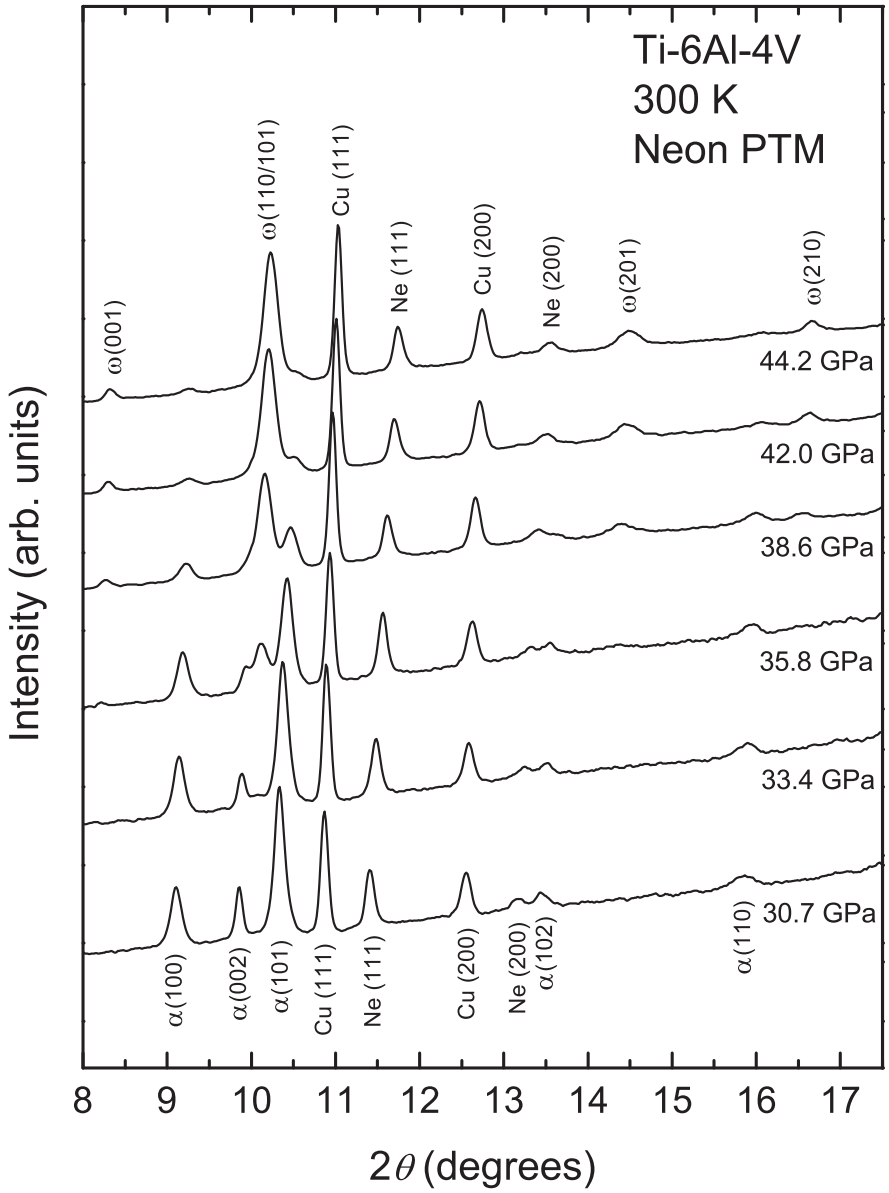

Figure 5.3: Diffraction profiles collected from Ti64 on compression from 30.7 GPa to 44.4 GPa in a neon pressure transmitting medium, showing the onset of the transition to the ω phase at 33.4 GPa. Diffraction peaks from the α and ω phases, and from the Cu pressure marker and the Ne pressure medium, are indexed. Figure reprinted from MacLeod *et al.* [MacLeod 12].

Table 5.1: The observed $\alpha \rightarrow \omega$ phase transition pressure, and the zero-pressure bulk modulus and its derivative, for Ti64 compressed in a number of different pressure transmitting media, as reported by MacLeod *et al.* [MacLeod 12]. The results obtained in previous studies [Chesnut 07, Halevy 10] are given for comparison.

Pressure medium	$P_{\alpha\rightarrow\omega}$ (GPa)	K_0 (GPa)	K'
No medium	32.1	151(4)	1.08(0.35)
Mineral oil	26.2	106(10)	5.07(1.23)
4:1 meth:eth	31.2	115(3)	3.22(0.22)
Neon	32.7	101(3)	4.05(0.29)
4:1 meth:eth [Chesnut 07]	27.3	125	2.41
No medium [Halevy 10]	Not observed	154(11)	5.45(1.44)

In three of the experiments, those using a neon PTM, mineral oil PTM and no PTM, a transformation was observed by MacLeod *et al.* from the ω phase to the bcc β phase above 94 GPa. This transition was not characterised by the appearance of new diffraction peaks, but rather by the gradual decrease in intensity, and subsequent disappearance, of the (001), (002) and (112) peaks from the ω phase. Figure 5.4 shows three diffraction patterns from Ti64 with a Cu pressure marker, but no PTM, collected at 106.3 GPa, 117.6 GPa and 127.1 GPa. At 106.3 GPa, 7 clear diffraction peaks from the ω phase were observed. On pressure increase to 117.6 GPa there was clear evidence for the decrease in intensity of the (001), (002) and (112) peaks. Further compression to 127.1 GPa virtually completed the transformation to the bcc β phase. Similar behaviour was observed in three different samples, with the transition to the β phase being complete between 115 GPa and 128 GPa. Again, these observed transition pressures are in good agreement with our calculations.

Furthermore, the observed volume change at the $\omega \rightarrow \beta$ transition was 0.6% for the neon PTM, 1.5% for the oil PTM and 1.6% for no PTM. This is in agreement with the $\omega \rightarrow \beta$ transition in Ti, where the bcc peaks are clearly displaced from the ω phase peaks and a two-phase refinement at 81 GPa revealed a density difference of 2% [Ahuja 04]; Zr, where the density difference between the ω and β phases at 30 GPa is 1.4% [Xia 90a]; and Hf, where there is a volume decrease of 2.1% at the $\omega \rightarrow \beta$ transition [Xia 90b].

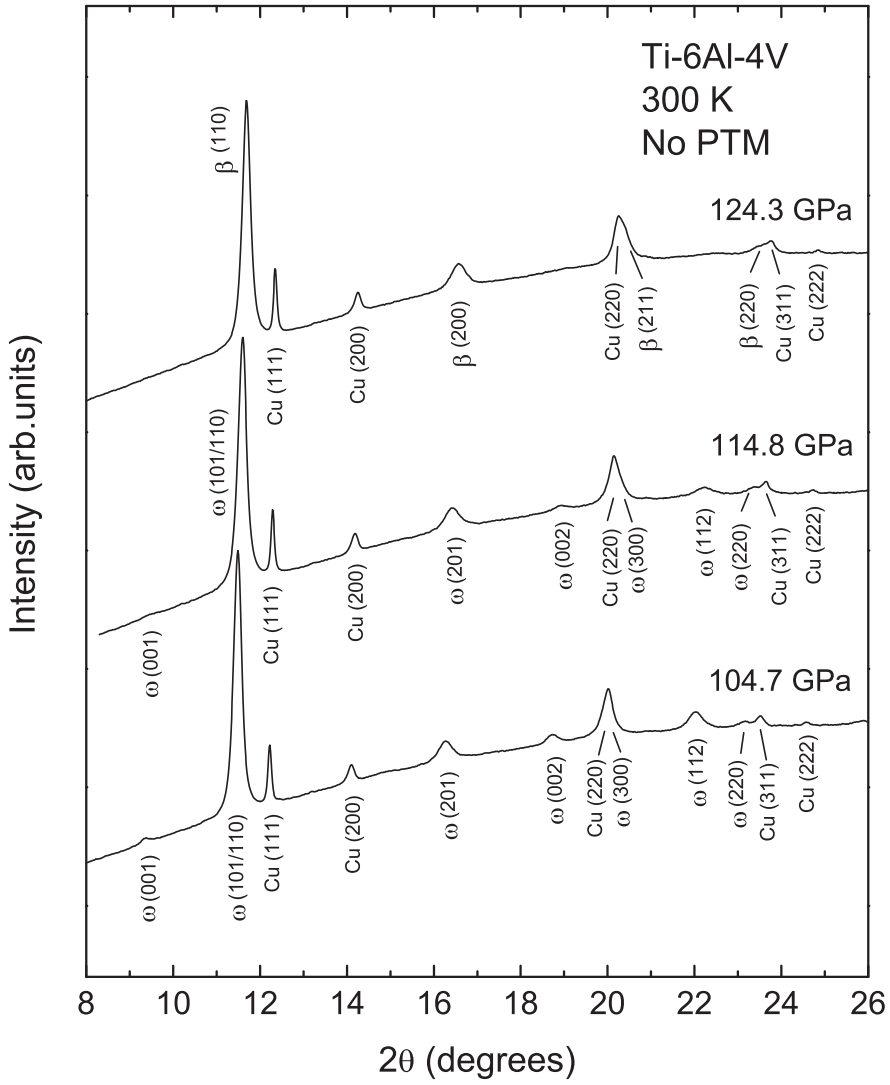

Figure 5.4: Diffraction profiles collected from Ti64 on compression from 106.3 GPa to 127.1 GPa without pressure transmitting medium, showing disappearance of the ω phase peaks that mark the transition from the hexagonal ω phase to the cubic β phase. Diffraction peaks from the ω phase and the Cu pressure marker are indexed in the 106.3 GPa profile, and peaks from the β phase are indexed in the 127.1 GPa profile. Figure reprinted from MacLeod *et al.* [MacLeod 12].

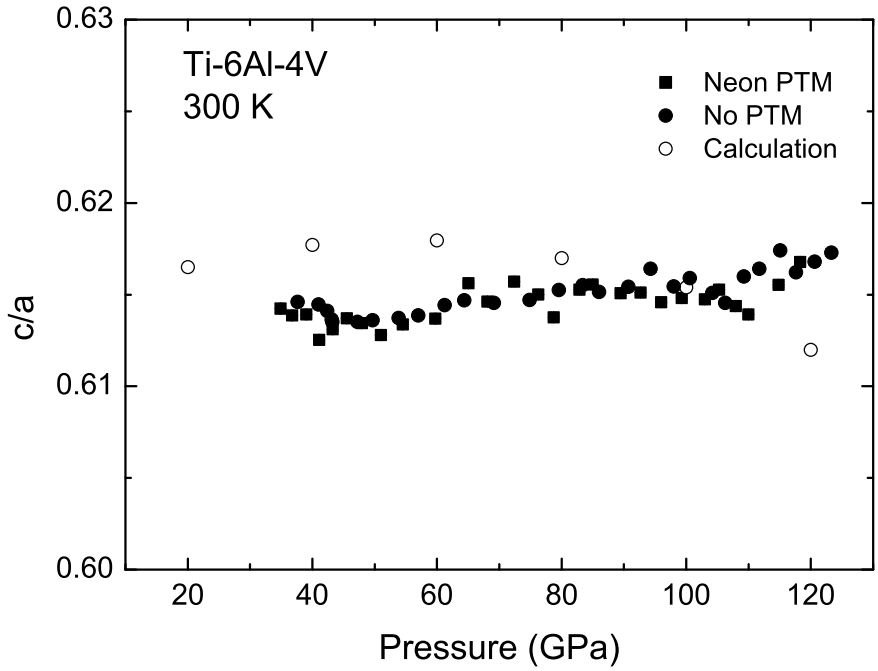

Figure 5.5: Pressure dependence of the c/a ratio for the hexagonal ω phase of Ti64, as obtained by MacLeod *et al.* [MacLeod 12], using the least (no PTM) and the most (neon PTM) hydrostatic compression experiments. The calculated c/a ratio, assuming local ordering of the Al and V atoms, is shown for comparison.

For those experiments above 100 GPa, the pressure was increased in steps smaller than 5 GPa to ensure the detection of any intermediate phases. No evidence was found by MacLeod *et al.* for the orthorhombic γ and δ phases reported by others in pure Ti [Vohra 01, Akahama 01], only the cubic β phase was observed, which was found to be stable to at least 221 GPa. This again is in agreement with our calculations.

Additionally, figure 5.5, shows the observed c/a axial ratio for the hexagonal ω phase over its full stability range from ∼30 to ∼125 GPa. The results, obtained by MacLeod *et al.*, using no PTM and a neon PTM, are identical. The axial ratio exhibits only a very small variation with pressure, and remains close to the ideal value of $\sqrt{3/8} = 0.612$. As a result, the unit cell is pseudo-cubic, and the d-spacings of the (110) and (101) peaks from the ω phase are almost identical at all pressures. The combined diffraction peaks thus remain unresolved to the highest pressures (see Fig. 5.4). Similar pressure independence of the c/a ratio of the ω phase was noted previously in Zr [Xia 90a], although the c/a ratio of

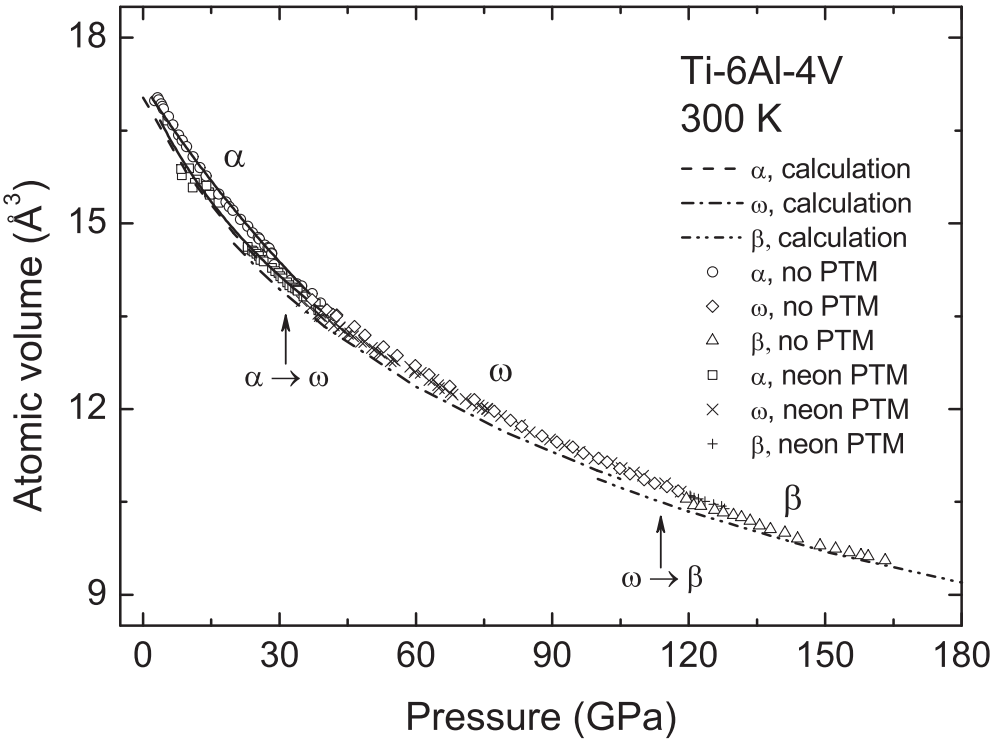

Figure 5.6: The compressibility of Ti64 to 175 GPa at room temperature, as determined from the sample with no PTM, and the sample with a neon PTM. The solid line shows the Vinet fit [Vinet 87] to the α phase data, as reported by MacLeod *et al.* [MacLeod 12]. The dashed lines shows our calculated data at 0 K, excluding thermal expansion.

0.625(2), was further from the ideal value.

Finally, figure 5.6 shows the experimental P-V data by MacLeod *et al.* [MacLeod 12] for Ti64 in a neon PTM and with no PTM present. The pressures at which the $\alpha \rightarrow \omega$ and $\omega \rightarrow \beta$ phase transitions were detected are marked with arrows. For comparison, the dashed lines show our calculated data, excluding thermal expansion.

5.5 Conclusions

In conclusion, we find that on compression, TI64 transforms from the hcp α phase at ambient pressure to the hexagonal ω phase at a pressure of around 25 GPa, much higher than for pure Ti (5 – 10 GPa), due to the presence of aluminium,

an α stabiliser. This ω phase remains stable until about 105 GPa, where it transforms to the the cubic β phase. Unlike for pure Ti, we find no evidence in our calculations on Ti64 for the orthorhombic γ and δ phases previously reported [Vohra 01, Akahama 01]. Both these results are in excellent agreement with the experimental results by MacLeod *et al.* [MacLeod 12].

However, we have also found that local ordering of atoms in Ti64 has significant effect on the transition pressures. DFT calculations of the $\alpha \rightarrow \omega$ and $\omega \rightarrow \beta$ transition pressures are in good agreement with the experimental values only when alloying atoms are placed as far apart as possible. This ordering is primarily a volume effect due to oversized Al impurities, and is only enthalpically favoured at high pressure. We take this as evidence that pressure-induced local ordering is occurring in the high-pressure experimental samples.

That said, there is no thermodynamic driving force for local ordering at ambient pressure, and the experimental samples studied by MacLeod *et al.* [MacLeod 12] were produced by rapid cooling from high temperature. Together, this implies that the local ordering should not have been present in the initial material. Rather, it must be created by atomic-level diffusion as the thermodynamic driving force is increased with applied pressure. Although this local diffusion occurs on the time-scale of the experiment, full phase separation to thermodynamic equilibrium does not.

Moreover, in contrast to a previous study [Chesnut 07], MacLeod *et al.* [MacLeod 12] also observed the coexistence of the α and ω phases of Ti64 over a large pressure range, similar to what Errandonea *et al.* reported for pure Ti [Errandonea 05]. Thermodynamically, it should not be possible to have a coexistence of phases with the same chemical composition over a range of hydrostatic pressures. The observation of phase coexistence is not uncommon in DAC experiments and could well be a consequence of non-hydrostatic conditions, even when using a PTM such as neon. Our calculations suggest another possibility; namely, that the transition is not thermodynamically favoured in the absence of local ordering. Thus, the martensitic reconstruction mechanism proposed by Trinkle *et al.* [Trinkle 03] cannot operate, and the preferred TAO-1 pathway is not accessible. Therefore, the transition must take place via a much slower diffusional mechanism. The coexistence of two phases after crossing a phase boundary may also be indicative of a metastable coexistence of the two

phases due to kinetics. A further hypothesis, based on the thermodynamic equilibrium, is that the coexistence is due to different chemical compositions in the two phases with a higher vanadium concentration stabilising the β phase. This would require significantly more diffusion than needed for local ordering, but this appears to be ruled out by the sample recovery at ambient pressure [MacLeod 12].

Chapter 6

Computational High-Pressure Studies of Ti Alloys

6.1 Introduction

Recently, new titanium alloys for particular applications have been developed, where commonly-used alloying elements such as vanadium and tin have been replaced with molybdenum and zirconium to facilitate better biocompatibility [Niinomi 98] or easier machinability [Siemers 09]. Molybdenum replaces vanadium as the main β-stabiliser in these alloys whereas zirconium replaces tin as a neutral solid solution strengthener.

This chapter focuses on two such alloys; the beta alloy Ti-Beta-21S, containing 15 wt.% Mo, 3 wt.% Nb, 3 wt.% Al, 0.2 wt.% Si and 78.8 wt.% Ti, which was developed as a corrosion resistant alternative for high-temperature aerospace applications [Boyer 96], and the prototype alpha-beta alloy Ti-676, containing 6 wt.% Al, 7 wt.% Zr, 6 wt.% Mo and 81 wt.% Ti, which is currently being developed as an easier to machine alternative to the existing alloy Ti-6Al-2Sn-4Zr-6Mo (Ti-6246) for machined aerospace components.

Furthermore, whilst the high pressure behaviour of pure titanium has been extensively studied previously [Joshi 02, Kutepov 03, Ahuja 04, Verma 07, Hao 08, Mei 09b, Hu 10], with Ti undergoing the $\alpha \rightarrow \omega \rightarrow \gamma \rightarrow \beta$ sequence of phase transformations with increasing pressure, the behaviour of titanium alloys is much less well established.

The main task of this work is to investigate the high pressure behaviour of

these two alloys using electronic structure calculations, and compare these results with our previous work on pure titanium and the alloy Ti-6Al-4V, (chapter 5), and with experimental results when available.

6.2 Computational Method

In order to explore the high-pressure behaviour of the molybdenum-containing titanium alloys Ti-676 and Ti-Beta-21S, we created two sets of computational samples, one for each composition, all using 54 atom supercells for the α, β and ω phases, and all having their alloying elements distributed as far apart as possible, following the same argument as in chapter 5. A bcc supercell for each alloy is shown in figure 6.1, with each alloying atom labelled and shown in a different colour. The upper panel shows Ti-676 and the lower panel shows Ti-Beta-21S. The unlabelled atoms are Ti in both cases.

As indicated in figure 6.1, the Ti-676 supercell has the following composition: 6 atoms of Al, 2 atoms of Zr, 2 atoms of Mo and 44 atoms of Ti, corresponding to 6.1 wt.% Al, 6.9 wt.% Zr, 7.3 wt.% Mo and 79.7 wt.% Ti. Similarly, the Ti-Beta-21S supercell has the following composition: 4 atoms of Mo, 3 atom of Al, 1 atom of Nb and 46 atoms of Ti, corresponding to 13.9 wt.% Mo, 2.9 wt.% Al, 3.4 wt.% Nb and 79.8 wt.% Ti. The 0.2wt.% Si content present in the commercial alloy was omitted to keep the computational cost down, on the basis that the silicon is added for improved creep resistance [Boyer 96] rather than acting as a phase stabiliser.

The calculations were performed using the DFT-code CASTEP [Clark 05], as described in chapter 2 using a k-point grid density of 0.05 Å^{-1}, a plane-wave cut-off of 500 eV and using the PBE generalised gradient approximation [Perdew 96] for the exchange-correlation.

6.3 Results

The calculated enthalpy curves at T = 0 K for the two alloys are shown in figure 6.2, with the upper panel showing Ti-676 and the lower panel showing Ti-Beta-21S. Both alloys seem to favour the body-centred β phase at zero pressure, in good agreement with the beta-stabilising effect of molybdenum

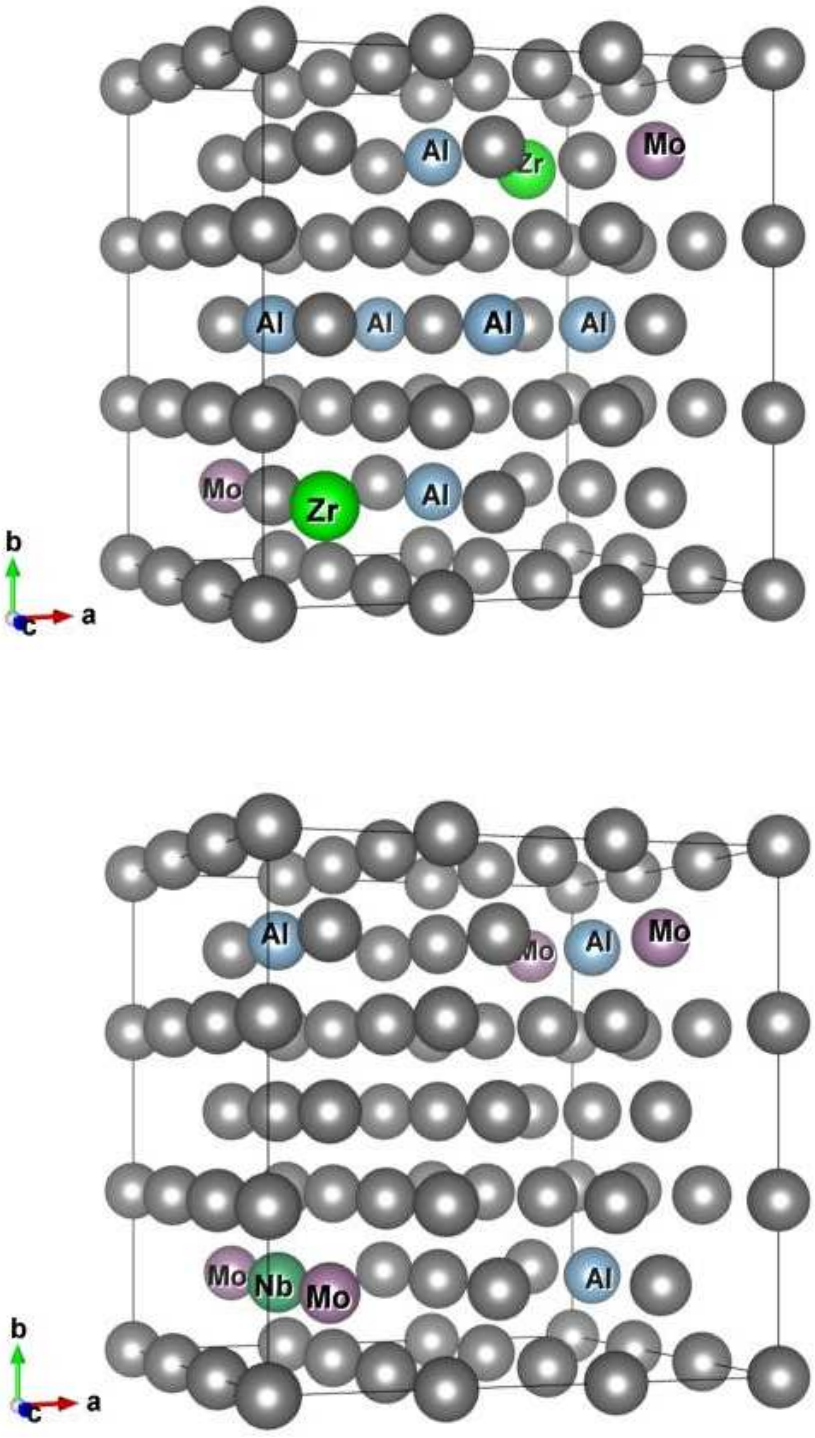

Figure 6.1: BCC supercells for the two Ti alloys, showing the position of each alloying element. The upper panel shows Ti-676, the lower panel shows Ti-Beta-21S. The unlabelled atoms are Ti.

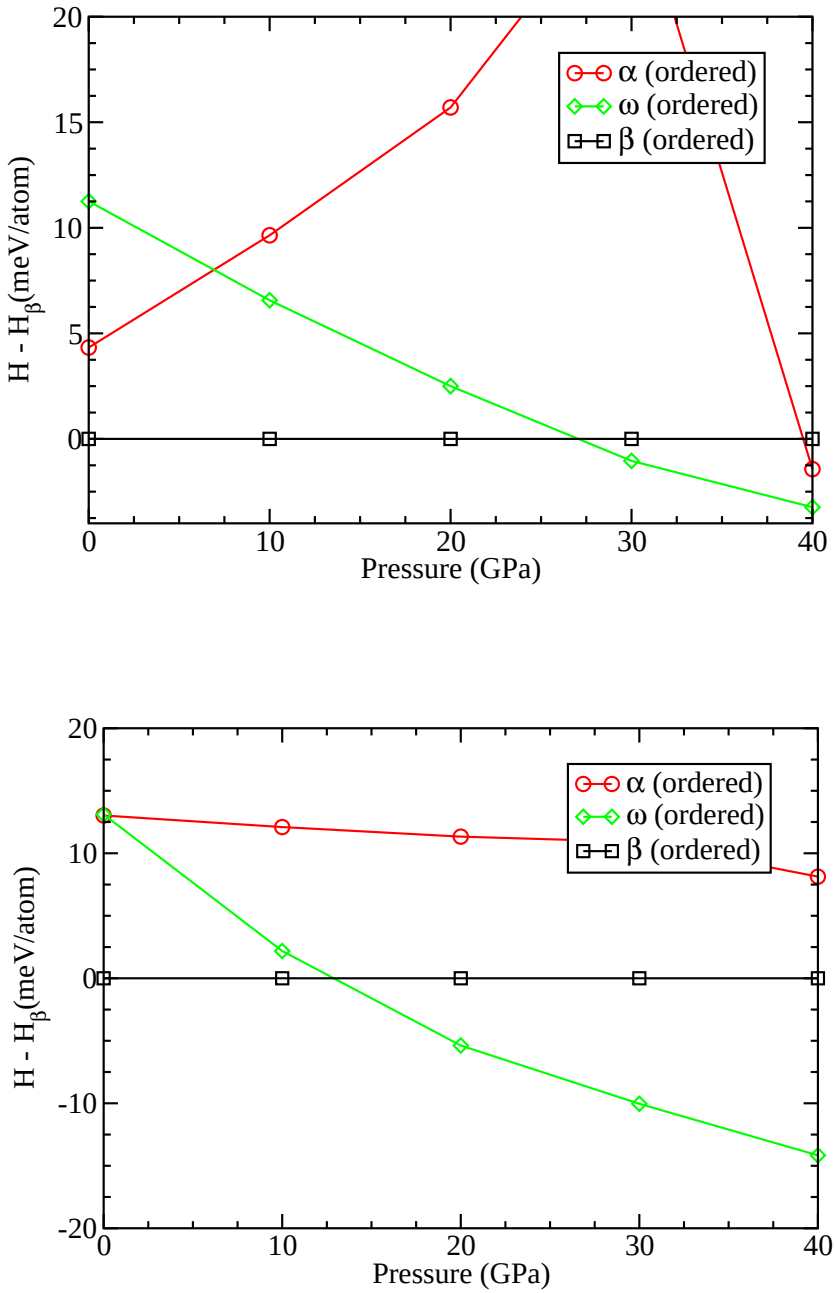

Figure 6.2: The calculated enthalpy differences at $T = 0$K between the α and ω phases, relative to that of the β phase, as a function of increasing pressure. The transition pressures are taken from where the lower curves cross. The upper graph shows the curve for Ti-676, the lower graph is the curve for Ti-Beta-21S. Both graphs assume that the alloying atoms are distributed as far apart as possible. The rightmost point on the upper α phase line at 40 GPa is anomalous and should be disregarded, having relaxed almost to the β phase.

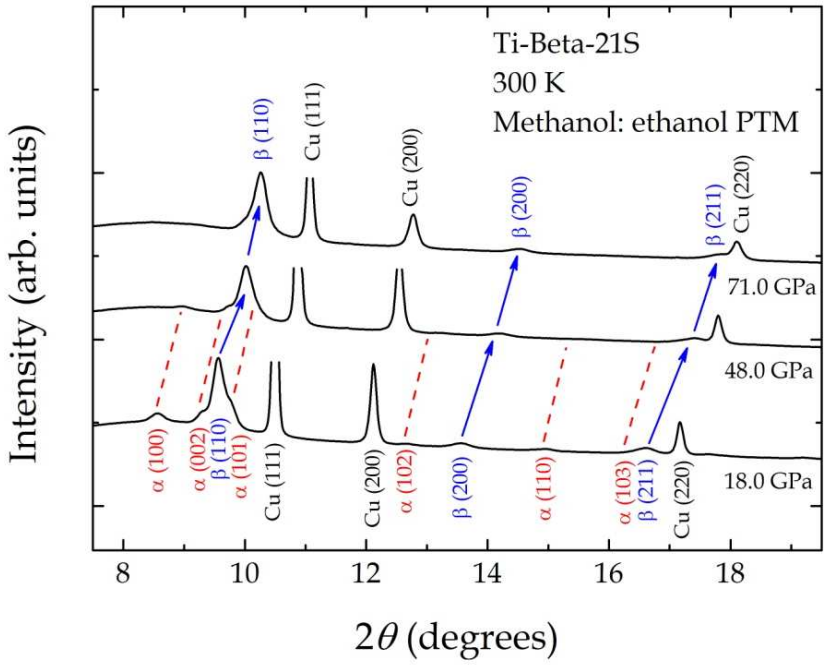

Figure 6.3: XRD spectra for Ti-Beta-21S, as reported by [Velisavljevic 07]. Figure reprinted from [Velisavljevic 12].

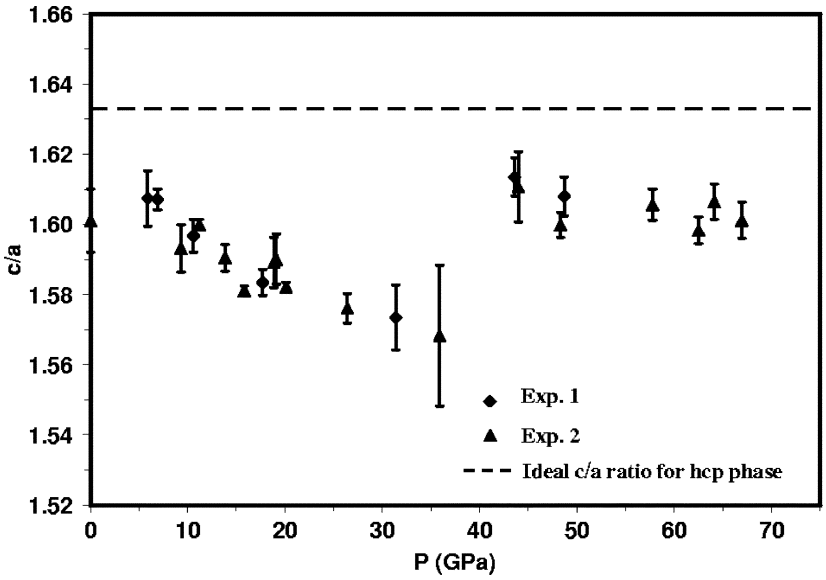

Figure 6.4: Change in c/a ratio of the α phase of Ti-Beta-21S with increasing pressure. Figure reprinted from [Velisavljevic 07].

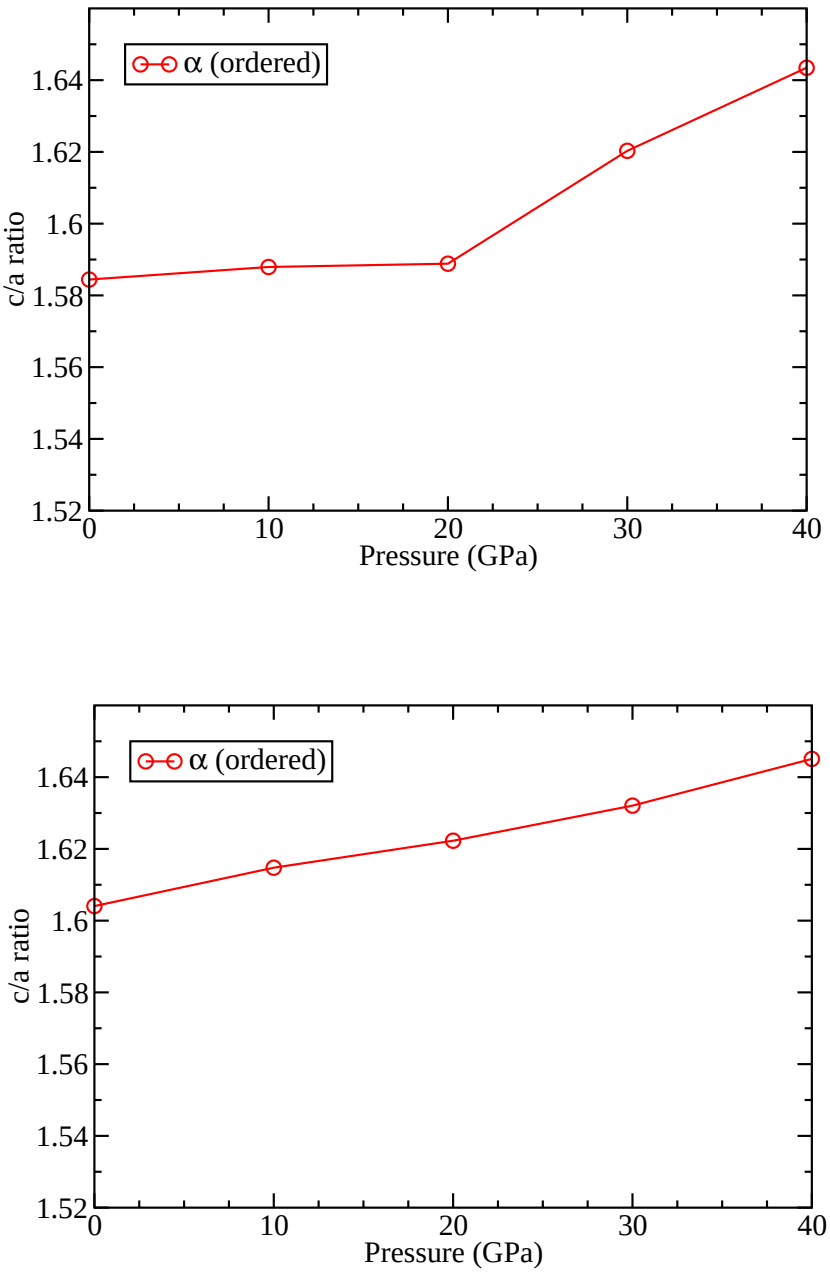

Figure 6.5: The calculated c/a ratio for the α phase, as a function of increasing pressure. The upper graph shows the curve for Ti-676, the lower graph is the curve for Ti-Beta-21S. Both graphs assume that the alloying atoms are distributed as far apart as possible. As in figure 6.2, the rightmost point on the upper graph at 40 GPa is anomalous and should be disregarded.

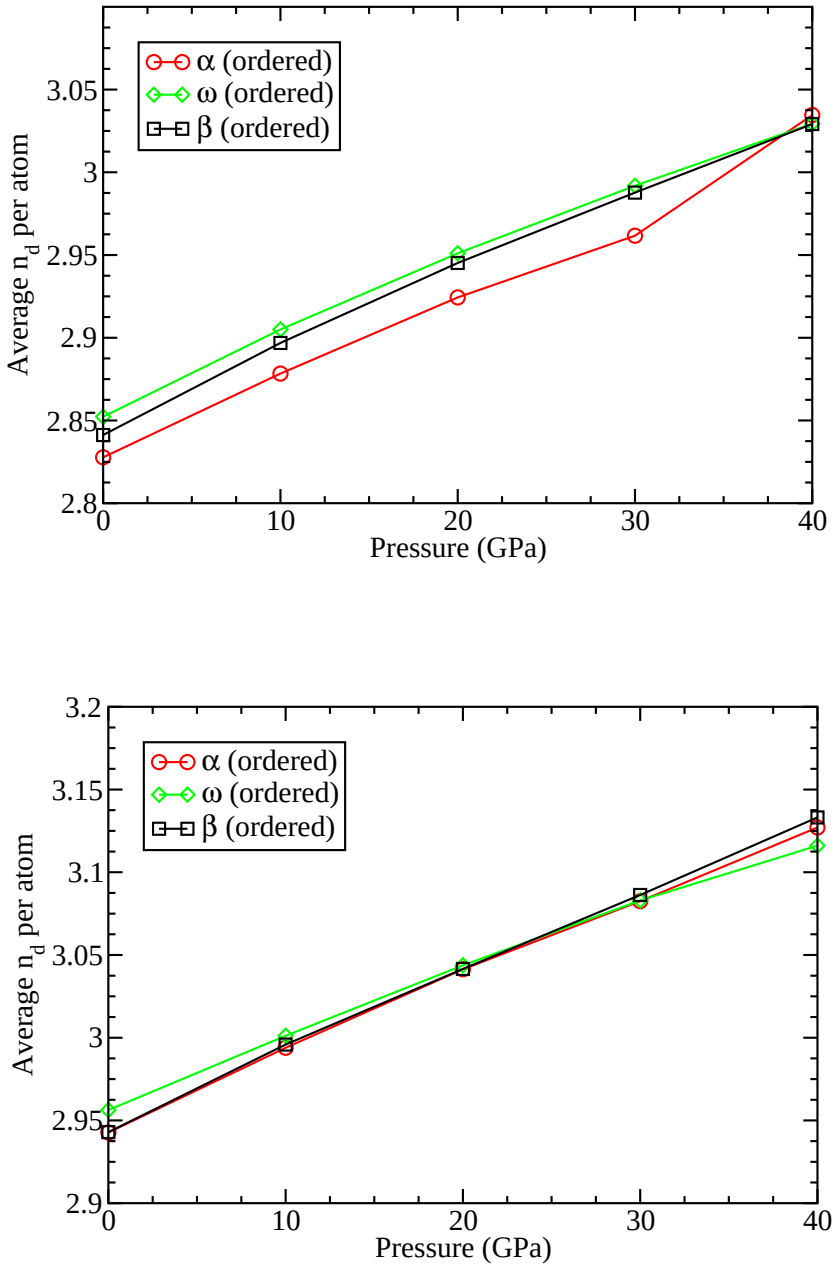

Figure 6.6: Average *d*-electron concentration as a function of increasing pressure for two different alloys. The upper graph shows Ti-676, the lower graph shows Ti-Beta-21S.

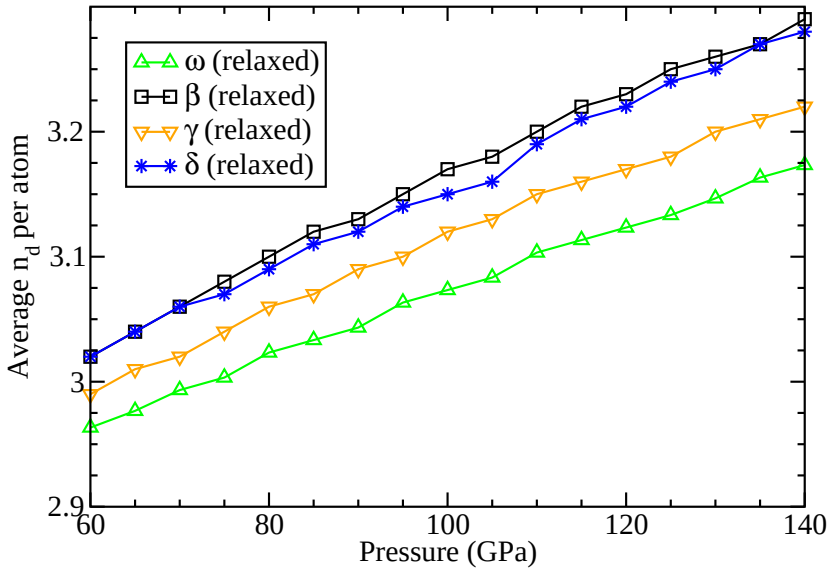

Figure 6.7: Average *d*-electron concentration as a function of increasing pressure for the high pressure phases of pure titanium.

Table 6.1: Calculated c/a ratios for different hcp Ti-Mo alloys, using results from chapter 4.

Composition	c/a ratio
Pure Ti	1.591
Ti + 8.33 at.% Mo	1.613
Ti + 16.67 at.% Mo	1.603
Ti + 25.00 at.% Mo	1.625

(chapter 4), but we expect entropy to also favour β at higher temperature. However upon compression, both alloys transform to the hexagonal ω phase, found experimentally as a meta-stable phase in Ti-Mo alloys [Hickman 69]. The transition pressure is about 27 GPa for Ti-676 and about 13 GPa for Ti-Beta-21S.

These results do not fit the pattern established for our earlier results, including our phase diagram in chapter 4, but there is some similarity with previous work on the element tantalum by Burakovsky *et al.* [Burakovsky 10], who report a bcc-omega phase transition at high pressure. The reason for this different result might be due to the presence of aluminium, or due to a poor choice of chemical decoration in the initial computational samples.

Moreover, our results also differ from experimental results by Velisavljevic *et al.* [Velisavljevic 07] on heat-treated Ti-Beta-21S. They report a direct hcp-bcc phase transition with pressure at RT, omitting the ω phase. One possible explanation for the missing ω phase may be due to segregation of the alloying elements during the heat treatment, leading to a mixture of molybdenum-enriched bcc phases and molybdenum-depleted hcp phases, both of unknown composition, in contrast to the well-mixed single phases of known composition used in our earlier calculations. The existence of such a phase mixture is predicted by the phase diagram in chapter 4 and is supported by the fact that the XRD spectra, shown in figure 6.3, show phase coexistence between the hcp and bcc phases. Additionally, the formation of the ω phase is known to be dependent on both composition and temperature [Hickman 69], conditions which may not be present in the experiment.

Furthermore, Velisavljevic *et al.* [Velisavljevic 07], report a significant change in the c/a ratio for the α phase of their heat-treated Ti-Beta-21S samples with increasing pressure. Their results are shown in figure 6.4. For comparison, the calculated c/a ratios for our alloys are shown in figure 6.5, where we only find a slight increase in the c/a ratio with increasing pressure, rather than a decrease. The reason for this difference might again be the heat treatment, where the different c/a ratios may be due to different Mo concentrations in each of the experimental samples. This is consistent with our earlier results on binary Ti alloys (chapter 4), which does show a change in the α phase c/a ratio with changing composition, as illustrated in table 6.1 for binary Ti-Mo alloys.

We now turn our attention to the underlying nature of the pressure induced

phase transition. Velisavljevic *et al.* [Velisavljevic 07] propose that increased d band occupancy with pressure acts a driving force for the transition. Figure 6.6 shows the average d-electron concentration as a function of pressure for Ti-676 (upper graph), and Ti-Beta-21S (lower graph), confirming that there is indeed some $s \rightarrow d$ transfer with pressure. Additionally, figure 6.7 shows the average d-electron occupancy for the high pressure phases of pure Ti. Comparing the figures, we find that they all have a similar slope, $\Delta P = 1/300 \Delta n_d$, suggesting a linear relation between pressure and $s \rightarrow d$ transfer for titanium and its alloys of similar valence. This surprising result allows us to rescale the x axis on our phase diagram shown in figure 4.5 to pressure, reinforcing our idea that it is the filling of the d-band that determines the phase stability of the transition metals, which can be altered by either alloying or pressure.

6.4 Conclusions

We have performed density functional studies on two Mo-containing Ti alloys, exploring their high-pressure behaviour. We find that in the ideal case of well-mixed alloys (rapidly quenched), they transform from the body-centred β phase to the hexagonal ω phase with increasing pressure, at 13 GPa and at 27 GPa, respectively. This is in agreement with previous work on high-pressure tantalum [Burakovsky 10], leading us to the suggestion of using Ti-Mo alloys to explore pressure-driven bcc to omega phase transitions and probe the properties of the mysterious ω phase.

However, these results differ from our general picture, including the phase diagram in chapter 4, which predicts a $\alpha \rightarrow \omega$ phase transition with increasing pressure, followed by a $\omega \rightarrow \beta$ transition, in contrast to the $\beta \rightarrow \omega$ transition found here. The source of this discrepancy might be due to the presence of aluminium or due to a poor sampling of chemical decorations used in the initial computational samples.

Moreover, our results also differ from experimental work [Velisavljevic 07] on heat-treated Ti-Beta-21S, but for a different reason. They report a direct hcp-bcc transition with pressure, omitting the ω phase. This may be due to compositional differences arising from the heat treatment, leading to a mixture of hcp and bcc phases with varying composition, suppressing the formation of the ω phase at

room temperature. Furthermore, these differences in composition would also explain the changes in the α phase c/a ratio observed in the experiment, which is consistent with our earlier work on binary Ti alloys (chapter 4), which show a small change in c/a ratio with changing composition.

That said, we do find a simple relationship between $s \rightarrow d$ transfer and pressure for our investigated alloys, which confirms earlier ideas that it is mainly the d-band filling that governs the phase stability of the transition metals and their alloys. This allows us to quantify the effects of alloying and pressure into a single parameter, the d-electron concentration.

In summary, further experimental investigations into the high-pressure behaviour of complex Ti alloys of known composition, supported by careful computational studies, are likely needed to explain these phenomena.

Chapter 7

Conclusions

7.1 Titanium Pseudopotentials

First of all, we have shown that the effect of apparently arbitrary choices in the construction of the pseudopotential can strongly affect the results of atomic calculation, changing equilibrium volumes by up to 10% and changing the crystal structure. In the case of titanium, it is possible to associate some features of the solid with the choice of reference configuration.

The most striking result is that the stable crystal structure is pseudopotential dependent. At 0 K, all the 12-electron potentials have the ω phase as the most stable, while the 4-electron ones have *hcp*. For pseudopotentials generated with a $3d^1 4s^2 4p^1$ configuration, the calculated $hcp \rightarrow \omega$ transition pressures are -2 GPa and +17 GPa respectively. The corresponding *hcp* volumes per atom are 17.76 Å^3 and 16.24 Å^3 respectively. In part this is related to the overestimation of the volume by the 4-electron potentials: but since the experimental volume (17.55 Å^3 per atom, [Trinité 08]), requires an external pressure of about 5 GPa for the volumes to match, this does not account for the whole effect.

Furthermore, all-electron calculations on Ti give the ω phase as the most stable [Ahuja 93], which is in agreement with our 12-electron pseudopotential results, thus validating our approach as a sensible approximation.

The study also underlines some of the large errors associated with the pseudopotential method, and the impressive way that these errors cancel in some cases. For reasonable choices of reference state, the eigenvalues of the atomic reference state can vary by several tenths of an eV. These are faithfully reproduced

by the pseudopotential, implying that the band structure isn't affected by the choice of reference state.

The results also cast serious doubt on the use of *spd*-projected densities of states for quantitative understanding, as these quantities are much more dependent on arbitrary choices in the pseudopotential than on the crystal structure itself.

7.2 Binary Titanium Alloys

In conclusion, we are considering ideal alloys produced by rapid quenching, and therefore unable to phase-separate to the thermodynamic equilibrium. We find that chromium and vanadium stabilise the β phase, while scandium destabilises it. The strength of the effect is directly proportional to the additional d-electrons present in the alloying element. The effect appears to be additive, and the positional effects of the impurities appear to be small, as evidenced by the small error bars in the inset of figure 4.1.

In the case of aluminium, our calculations show that it stabilises the α phase and destabilises the β phase, but the simple d-electron sum rule does not apply to this *sp* element.

While the correct stabilisation predictions of pseudopotential calculations are unsurprising, we have also tested our hypothesis by comparing it with VCA and extra-electron calculations, which correctly capture the aspects of the physics we think are important. The accurate results obtained from these normally unreliable methods give strong support to the d-electron picture.

This puts the empirically known effects of α and β stabilisation on a firm theoretical footing. It also enables alloy designers to anticipate the phase-stabilising effects of additions which may be added for other purposes. Finally, it emphasises the need for the d-electron concentration to be considered as a parameter in any multi-scale modelling approach.

7.3 Titanium and Ti Alloys under Pressure

7.3.1 Ti-6Al-4V

In conclusion, we find that on compression, TI64 transforms from the hcp α phase at ambient pressure to the hexagonal ω phase at a pressure of around 25 GPa, much higher than for pure Ti (5 – 10 GPa), due to the presence of aluminium, an α stabiliser. This ω phase remains stable until about 105 GPa, where it transforms to the the cubic β phase. Unlike for pure Ti, we find no evidence in our calculations on Ti64 for the orthorhombic γ and δ phases previously reported [Vohra 01, Akahama 01]. Both these results are in excellent agreement with the experimental results by MacLeod *et al.* [MacLeod 12].

However, we have also found that local ordering of atoms in Ti64 has significant effect on the transition pressures. DFT calculations of the $\alpha \rightarrow \omega$ and $\omega \rightarrow \beta$ transition pressures are in good agreement with the experimental values only when alloying atoms are placed as far apart as possible. This ordering is primarily a volume effect due to oversized Al impurities, and is only enthalpically favoured at high pressure. We take this as evidence that pressure-induced local ordering is occurring in the high-pressure experimental samples.

That said, there is no thermodynamic driving force for local ordering at ambient pressure, and the experimental samples studied by MacLeod *et al.* [MacLeod 12] were produced by rapid cooling from high temperature. Together, this implies that the local ordering should not have been present in the initial material. Rather, it must be created by atomic-level diffusion as the thermodynamic driving force is increased with applied pressure. Although this local diffusion occurs on the time-scale of the experiment, full phase separation to thermodynamic equilibrium does not.

Moreover, in contrast to a previous study [Chesnut 07], MacLeod *et al.* [MacLeod 12] also observed the coexistence of the α and ω phases of Ti64 over a large pressure range, similar to what Errandonea *et al.* reported for pure Ti [Errandonea 05]. Thermodynamically, it should not be possible to have a coexistence of phases with the same chemical composition over a range of hydrostatic pressures. The observation of phase coexistence is not uncommon in DAC experiments and could well be a consequence of non-hydrostatic conditions, even when using a PTM such as neon. Our calculations suggest another

possibility; namely, that the transition is not thermodynamically favoured in the absence of local ordering. Thus, the martensitic reconstruction mechanism proposed by Trinkle *et al.* [Trinkle 03] cannot operate, and the preferred TAO-1 pathway is not accessible. Therefore, the transition must take place via a much slower diffusional mechanism. The coexistence of two phases after crossing a phase boundary may also be indicative of a metastable coexistence of the two phases due to kinetics. A further hypothesis, based on the thermodynamic equilibrium, is that the coexistence is due to different chemical compositions in the two phases with a higher vanadium concentration stabilising the β phase. This would require significantly more diffusion than needed for local ordering, but this appears to be ruled out by the sample recovery at ambient pressure [MacLeod 12].

7.3.2 Ti-Mo Alloys

We have performed density functional studies on two Mo-containing Ti alloys, exploring their high-pressure behaviour. We find that in the ideal case of well-mixed alloys, they transform from the body-centred β phase to the hexagonal ω phase with increasing pressure, at 13 GPa and at 27 GPa respectively. This is in agreement with previous work on high-pressure tantalum [Burakovsky 10], leading us to the suggestion of using Ti-Mo alloys to explore pressure-driven bcc to omega phase transitions and probe the properties of the mysterious ω phase.

However, these results do not fit with our general picture, including the phase diagram in chapter 4, which predicts a $\alpha \rightarrow \omega$ phase transition with increasing pressure, followed by a $\omega \rightarrow \beta$ transition, in contrast to the $\beta \rightarrow \omega$ transition found here. The source of this discrepancy might be due to the presence of aluminium or due to a poor sampling of chemical decorations in the initial computational samples.

Moreover, our results also differ from experimental work [Velisavljevic 07] on heat-treated Ti-Beta-21S, but for a different reason. They report a direct hcp-bcc transition with pressure, omitting the ω phase. This may be due to compositional differences arising from the heat treatment, leading to a mixture of hcp and bcc phases with varying composition, suppressing the formation of the ω phase at room temperature. Furthermore, these differences in composition would also explain the changes in the α phase c/a ratio observed in the experiment, which

is consistent with our earlier work on binary Ti alloys (chapter 4), which show a small change in c/a ratio with changing composition.

That said, we do find a simple relationship between $s \rightarrow d$ transfer and pressure for our investigated alloys, which confirms earlier ideas that it is mainly the d-band filling that governs the phase stability of the transition metals and their alloys. This allows us to quantify the effects of alloying and pressure into a single parameter, the d-electron concentration.

In summary, further experimental investigations into the high-pressure behaviour of complex Ti alloys of known composition, supported by careful computational studies, are likely needed to fully explain these phenomena.

Bibliography

[Ackland 02] G. J. Ackland. *Calculation of free energies from ab initio calculation.* Journal of Physics: Condensed Matter, vol. 14, no. 11, pages 2975–3000, 2002.

[Ahuja 93] Rajeev Ahuja, John M. Wills, Börje Johansson & Olle Eriksson. *Crystal structures of Ti, Zr, and Hf under compression: Theory.* Phys. Rev. B, vol. 48, no. 22, pages 16269–16279, December 1993.

[Ahuja 04] Rajeev Ahuja, Leonid Dubrovinsky, Natalia Dubrovinskaia, J. M. Osorio Guillen, Maurizio Mattesini, Börje Johansson & Tristan Le Bihan. *Titanium metal at high pressure: Synchrotron experiments and ab initio calculations.* Phys. Rev. B, vol. 69, no. 18, page 184102, May 2004.

[Akahama 01] Yuichi Akahama, Haruki Kawamura & Tristan Le Bihan. *New delta (Distorted-bcc) Titanium to 220 GPa.* Phys. Rev. Lett., vol. 87, no. 27, page 275503, December 2001.

[Andersen 77] O. K. Andersen & O. Jepsen. *Advances in the theory of one-electron energy states.* Physica B+C, vol. 91, pages 317–328, July 1977.

[Bachelet 82] G. B. Bachelet, D. R. Hamann & M. Schlüter. *Pseudopotentials that work: From H to Pu.* Phys. Rev. B, vol. 26, no. 8, pages 4199–4228, October 1982.

[Baroni 01] Stefano Baroni, Stefano de Gironcoli, Andrea Dal Corso & Paolo Giannozzi. *Phonons and related crystal properties from density-functional perturbation theory.* Rev. Mod. Phys., vol. 73, no. 2, pages 515–562, July 2001.

[Bellaiche 00] L. Bellaiche & David Vanderbilt. *Virtual crystal approximation revisited: Application to dielectric and piezoelectric properties of perovskites.* Phys. Rev. B, vol. 61, no. 12, pages 7877–7882, March 2000.

[Blöchl 94] P. E. Blöchl. *Projector augmented-wave method.* Phys. Rev. B, vol. 50, no. 24, pages 17953–17979, December 1994.

[Booth 13] George H. Booth, Andreas Gruneis, Georg Kresse & Ali Alavi. *Towards an exact description of electronic wavefunctions in real solids.* Nature, vol. 493, no. 7432, pages 365–370, January 2013.

[Boyer 96] R. R. Boyer. *An overview on the use of titanium in the aerospace industry.* Materials Science and Engineering: A, vol. 213, no. 1-2, pages 103–114, August 1996.

[Burakovsky 10] L. Burakovsky, S. P. Chen, D. L. Preston, A. B. Belonoshko, A. Rosengren, A. S. Mikhaylushkin, S. I. Simak & J. A. Moriarty. *High-PressureHigh-Temperature Polymorphism in Ta: Resolving an Ongoing Experimental Controversy.* Phys. Rev. Lett., vol. 104, no. 25, page 255702, June 2010.

[Ceperley 80] D. M. Ceperley & B. J. Alder. *Ground State of the Electron Gas by a Stochastic Method.* Phys. Rev. Lett., vol. 45, no. 7, pages 566–569, August 1980.

[Chen 01] Q. Chen & B. Sundman. *Calculation of debye temperature for crystalline structures–a case study on Ti, Zr, and Hf.* Acta Materialia, vol. 49, no. 6, pages 947–961, April 2001.

[Chesnut 07] Gary N. Chesnut, Nenad Velisavljevic & Lilliana Sanchez. *STATIC HIGH PRESSURE X-RAY DIFFRACTION OF TI-6AL-4V.* AIP Conf. Proc., vol. 955, no. 1, pages 27–30, December 2007.

[Clark 05] Stewart J. Clark, Matthew D. Segall, Chris J. Pickard, Phil J. Hasnip, Matt I. J. Probert, Keith Refson & Mike C. Payne. *First principles methods using CASTEP.* Zeitschrift für Kristallographie, vol. 220, no. 5-6-2005, pages 567–570, May 2005.

[Collings 84] E. W. Collings. The physical metallurgy of titanium alloys. American Society for Metals, Metals Park, 1984.

[Dewaele 04] Agnès Dewaele, Paul Loubeyre & Mohamed Mezouar. *Equations of state of six metals above 94GPa.* Phys. Rev. B, vol. 70, no. 9, page 094112, September 2004.

[Dewaele 08] Agnès Dewaele, Frdric Datchi, Paul Loubeyre & Mohamed Mezouar. *High pressure-high temperature equations of state of neon and diamond.* Phys. Rev. B, vol. 77, no. 9, page 094106, March 2008.

[Errandonea 05] Daniel Errandonea, Y. Meng, M. Somayazulu & D. Häusermann. *Pressure-induced $\alpha \rightarrow \omega$ transition in titanium metal: a systematic study of the effects of uniaxial stress.* Physica B: Condensed Matter, vol. 355, no. 1-4, pages 116–125, January 2005.

[Gray 93] G. T. Gray, C. E. Morris & A. C. Lawson. Proceedings of titanium 92: Science and technology. Minerals, Metals, and Materials Society, Warrendale, 1993.

[Gunnarsson 76] O. Gunnarsson & B. I. Lundqvist. *Exchange and correlation in atoms, molecules, and solids by the spin-density-functional formalism.* Phys. Rev. B, vol. 13, no. 10, pages 4274–4298, May 1976.

[Haken 05] H. Haken & H. C. Wolf. The physics of atoms and quanta: Introduction to experiments and theory. Advanced Texts in Physics. Springer, 2005.

[Halevy 10] I. Halevy, G. Zamir, M. Winterrose, G. Sanjit, Carlos Roberto Grandini & Ariel Moreno-Gobbi. *Crystallographic structure of Ti-6Al-4V, Ti-HP and Ti-CP under high-pressure.* Journal of Physics: Conference Series, vol. 215, no. 1, page 012013, 2010.

[Hamann 79] D. R. Hamann, M. Schlüter & C. Chiang. *Norm-Conserving Pseudopotentials.* Phys. Rev. Lett., vol. 43, no. 20, pages 1494–1497, November 1979.

[Hao 08] Yan-Jun Hao, Lin Zhang, Xiang-Rong Chen, Ying-Hua Li & Hong-Liang He. *First-principles phase transition and equation of state of titanium.* Solid State Communications, vol. 146, no. 3-4, pages 105–109, April 2008.

[Hart 12] Gus L. W. Hart. *Computational materials science: Substitution with vision.* Nature, vol. 491, no. 7426, pages 674–675, November 2012.

[Hayes 95] F. Hayes. *The Al-Ti-V (aluminum-titanium-vanadium) system.* Journal of Phase Equilibria, vol. 16, no. 2, pages 163–176, 1995.

[Hedin 71] L. Hedin & B. I. Lundqvist. *Explicit local exchange-correlation potentials.* Journal of Physics C: Solid State Physics, vol. 4, no. 14, pages 2064–2083, 1971.

[Hennig 05] Richard G. Hennig, Dallas R. Trinkle, Johann Bouchet, Srivilliputhur G. Srinivasan, Robert C. Albers & John W. Wilkins. *Impurities block the [alpha] to [omega] martensitic transformation in titanium.* Nat Mater, vol. 4, no. 2, pages 129–133, February 2005.

[Hennig 08] R. G. Hennig, T. J. Lenosky, D. R. Trinkle, S. P. Rudin & J. W. Wilkins. *Classical potential describes martensitic phase transformations between the alpha , beta , and omega titanium phases.* Phys. Rev. B, vol. 78, no. 5, page 054121, August 2008.

[Hickman 69] B. S. Hickman. *The formation of omega phase in titanium and zirconium alloys: A review.* Journal of Materials Science, vol. 4, no. 6, pages 554–563, June 1969.

[Hohenberg 64] P. Hohenberg & W. Kohn. *Inhomogeneous Electron Gas.* Phys. Rev., vol. 136, no. 3B, pages B864–B871, Nov 1964.

[Hu 08] Qing-Miao Hu, Shu-Jun Li, Yu-Lin Hao, Rui Yang, Börje Johansson & Levente Vitos. *Phase stability and elastic modulus of Ti alloys containing Nb, Zr, and/or Sn from first-principles calculations.* Appl. Phys. Lett., vol. 93, no. 12, page 121902, September 2008.

[Hu 10] Cui-E Hu, Zhao-Yi Zeng, Lin Zhang, Xiang-Rong Chen, Ling-Cang Cai & Dario Alfè. *Theoretical investigation of the high pressure structure, lattice dynamics, phase transition, and thermal equation of state of titanium metal.* J. Appl. Phys., vol. 107, no. 9, page 093509, May 2010.

[Hume-Rothery 34] William Hume-Rothery, Gilbert W. Mabbott & K. M. Channel Evans. *The Freezing Points, Melting Points, and Solid Solubility Limits of the Alloys of Silver, and Copper with the Elements of the B Sub-Groups.* Philosophical Transactions of the Royal Society of London. Series A, Containing Papers of a Mathematical or Physical Character, vol. 233, no. 721-730, pages 1–97, January 1934.

[Hume-Rothery 50] William Hume-Rothery. The structure of metals and alloys. The Institute of Metals, London, 1950.

[Ikehata 04] Hideaki Ikehata, Naoyuki Nagasako, Tadahiko Furuta, Atsuo Fukumoto, Kazutoshi Miwa & Takashi Saito. *First-principles calculations for development of low elastic modulus Ti alloys.* Phys. Rev. B, vol. 70, no. 17, page 174113, November 2004.

[Joshi 02] K. D. Joshi, G. Jyoti, Satish C. Gupta & S. K. Sikka. *Stability of gamma and delta phases in Ti at high pressures.* Phys. Rev. B, vol. 65, no. 5, page 052106, January 2002.

[Kerker 80] G. P. Kerker. *Non-singular atomic pseudopotentials for solid state applications.* Journal of Physics C: Solid State Physics, vol. 13, no. 9, page L189, 1980.

[Kleinman 82] Leonard Kleinman & D. M. Bylander. *Efficacious Form for Model Pseudopotentials.* Phys. Rev. Lett., vol. 48, no. 20, pages 1425–1428, May 1982.

[Kohn 65] W. Kohn & L. J. Sham. *Self-Consistent Equations Including Exchange and Correlation Effects.* Phys. Rev., vol. 140, no. 4A, pages A1133–A1138, Nov 1965.

[Kutepov 03] A. L. Kutepov & S. G. Kutepova. *Crystal structures of Ti under high pressure: Theory.* Phys. Rev. B, vol. 67, no. 13, page 132102, April 2003.

[Laasonen 93] Kari Laasonen, Alfredo Pasquarello, Roberto Car, Changyol Lee & David Vanderbilt. *Car-Parrinello molecular dynamics with Vanderbilt ultrasoft pseudopotentials.* Phys. Rev. B, vol. 47, no. 16, pages 10142–10153, April 1993.

[Lazar 11] Petr Lazar, Michal Jahnátek, Jürgen Hafner, Naoyuki Nagasako, Ryoji Asahi, Claudia Blaas-Schenner, Markus Stöhr & Raimund Podloucky. *Temperature-induced martensitic phase transitions in gum-metal approximants: First-principles investigations for Ti3Nb.* Phys. Rev. B, vol. 84, no. 5, page 054202, August 2011.

[Li 07] Tianshu Li, J. W. Morris, Jr., N. Nagasako, S. Kuramoto & D. C. Chrzan. *Ideal Engineering Alloys.* Phys. Rev. Lett., vol. 98, no. 10, page 105503, March 2007.

[Lin 93] J. S. Lin, A. Qteish, M. C. Payne & V. Heine. *Optimized and transferable nonlocal separable ab initio pseudopotentials.* Phys. Rev. B, vol. 47, no. 8, pages 4174–4180, February 1993.

[Liu 08] H. Q. Liu, D. Q. Yi & F. Zheng. *The influence of Sc on [alpha]/[beta] transformation of Ti.* Materials Science and Engineering: A, vol. 487, no. 1–2, pages 58–63, July 2008.

[MacLeod 12] S. G. MacLeod, B. E. Tegner, H. Cynn, W. J. Evans, J. E. Proctor, M. I. McMahon & G. J. Ackland. *Experimental and theoretical study of Ti-6Al-4V to 220 GPa.* Phys. Rev. B, vol. 85, no. 22, page 224202, June 2012.

[Martin 04] Richard M. Martin. Electronic structure: Basic theory and practical methods. Cambridge University Press, 2004.

[Mattsson 05] Ann E. Mattsson, Peter A. Schultz, Michael P. Desjarlais, Thomas R. Mattsson & Kevin Leung. *Designing meaningful density functional theory calculations in materials sciencea primer.* Modelling and Simulation in Materials Science and Engineering, vol. 13, no. 1, pages R1–R31, 2005.

[Mei 09a] Zhi-Gang Mei, Shun-Li Shang, Yi Wang & Zi-Kui Liu. *Density-functional study of the thermodynamic properties and the pressure-temperature phase diagram of Ti.* Phys. Rev. B, vol. 80, no. 10, page 104116, September 2009.

[Mei 09b] Zhi-Gang Mei, ShunLi Shang, Yi Wang & Zi-Kui Liu. *Density-functional study of the pressure-induced phase transitions in Ti at zero Kelvin.* Phys. Rev. B, vol. 79, no. 13, page 134102, April 2009.

[Monkhorst 76] Hendrik J. Monkhorst & James D. Pack. *Special points for Brillouin-zone integrations.* Phys. Rev. B, vol. 13, no. 12, pages 5188–5192, June 1976.

[Moruzzi 88] V. L. Moruzzi, J. F. Janak & K. Schwarz. *Calculated thermal properties of metals.* Phys. Rev. B, vol. 37, no. 2, pages 790–799, January 1988.

[Needs 10] R. J. Needs, M. D. Towler, N. D. Drummond & P. López Ríos. *Continuum variational and diffusion quantum Monte Carlo calculations.* Journal of Physics: Condensed Matter, vol. 22, no. 2, page 023201, 2010.

[Nemec 10] Norbert Nemec, Michael D. Towler & R. J. Needs. *Benchmark all-electron ab initio quantum Monte Carlo calculations for small molecules.* J. Chem. Phys., vol. 132, no. 3, page 034111, January 2010.

[Niinomi 98] Mitsuo Niinomi. *Mechanical properties of biomedical titanium alloys.* Materials Science and Engineering: A, vol. 243, no. 1-2, pages 231–236, March 1998.

[Perdew 81] J. P. Perdew & Alex Zunger. *Self-interaction correction to density-functional approximations for many-electron systems.* Phys. Rev. B, vol. 23, no. 10, pages 5048–5079, May 1981.

[Perdew 92a] John P. Perdew, J. A. Chevary, S. H. Vosko, Koblar A. Jackson, Mark R. Pederson, D. J. Singh & Carlos Fiolhais. *Atoms, molecules, solids, and surfaces: Applications of the generalized gradient approximation for exchange and correlation.* Phys. Rev. B, vol. 46, no. 11, pages 6671–6687, September 1992.

[Perdew 92b] John P. Perdew & Yue Wang. *Accurate and simple analytic representation of the electron-gas correlation energy.* Phys. Rev. B, vol. 45, no. 23, pages 13244–13249, June 1992.

[Perdew 96] John P. Perdew, Kieron Burke & Matthias Ernzerhof. *Generalized Gradient Approximation Made Simple.* Phys. Rev. Lett., vol. 77, no. 18, pages 3865–3868, October 1996.

[Peters 03] M. Peters, J. Hemptenmacher, J. Kumpfert & C. Leyens. Titanium and titanium alloys: Fundamentals and applications. Wiley-VCH, Weinheim, 2003.

[Petry 91] W. Petry, A. Heiming, J. Trampenau, M. Alba, C. Herzig, H. R. Schober & G. Vogl. *Phonon dispersion of the bcc phase of group-IV metals. I. bcc titanium.* Phys. Rev. B, vol. 43, no. 13, pages 10933–10947, May 1991.

[Pettifor 70] D. G. Pettifor. *Theory of the crystal structures of transition metals.* Journal of Physics C: Solid State Physics, vol. 3, no. 2, pages 367–377, 1970.

[Pettifor 84] D. G. Pettifor. *A chemical scale for crystal-structure maps.* Solid State Communications, vol. 51, no. 1, pages 31–34, July 1984.

[Pettifor 86] D. G. Pettifor. *The structures of binary compounds. I. Phenomenological structure maps.* Journal of Physics C: Solid State Physics, vol. 19, no. 3, pages 285–313, 1986.

[Pettifor 95] D. G. Pettifor. Bonding and structure of molecules and solids. Oxford University Press, Oxford, 1995.

[Raabe 07] D. Raabe, B. Sander, M. Friak, D. Ma & J. Neugebauer. *Theory-guided bottom-up design of [beta]-titanium alloys as biomaterials based on first principles calculations: Theory and experiments.* Acta Materialia, vol. 55, no. 13, pages 4475–4487, August 2007.

[Rappe 90] Andrew M. Rappe, Karin M. Rabe, Efthimios Kaxiras & J. D. Joannopoulos. *Optimized pseudopotentials.* Phys. Rev. B, vol. 41, no. 2, pages 1227–1230, January 1990.

[Rosenberg 81] Z. Rosenberg, Y. Meybar & D. Yaziv. *Measurement of the Hugoniot curve of Ti-6Al-4V with commercial manganin gauges.* Journal of Physics D: Applied Physics, vol. 14, no. 2, pages 261–266, 1981.

[Rudin 04] Sven P. Rudin, M. D. Jones & R. C. Albers. *Thermal stabilization of the hcp phase in titanium.* Phys. Rev. B, vol. 69, no. 9, page 094117, March 2004.

[Sass 98] S. L. Sass. The substance of civilization: Materials and human history from the stone age to the age of silicon. Arcade Publishing, 1998.

[Savitskii 62] E. M. Savitskii & G. S. Burkhanov. *Phasen-diagramme von Titan-legierungen mit seltenen erdmetallen.* Journal of the Less Common Metals, vol. 4, no. 4, pages 301–314, August 1962.

[Siemers 09] C. Siemers, B. Zahra, T. Leemet & J. Rösler. *Development of Advanced beta-Titanium Alloys.* In Proceedings of the 8th AMMT09 Conference, St. Petersburg, Russia, June 24th 26th 2009, 2009.

[Souvatzis 08] P. Souvatzis, O. Eriksson, M. I. Katsnelson & S. P. Rudin. *Entropy Driven Stabilization of Energetically Unstable Crystal Structures Explained from First Principles Theory.* Phys. Rev. Lett., vol. 100, no. 9, page 095901, March 2008.

[Tane 10] M. Tane, S. Akita, T. Nakano, K. Hagihara, Y. Umakoshi, M. Niinomi, H. Mori & H. Nakajima. *Low Young's modulus of Ti-Nb-Ta-Zr alloys caused by softening in shear moduli c' and c44 near lower limit of body-centered cubic phase stability.* Acta Materialia, vol. 58, no. 20, pages 6790–6798, December 2010.

[Tegner 11] Bengt E. Tegner, Simon G. MacLeod, Hyunchae Cynn, John Proctor, William J. Evans, Malcolm I. McMahon & Graeme J. Ackland. *An Experimental and Theoretical Multi-Mbar Study of Ti-6Al-4V.* MRS Online Proceedings Library, vol. 1369, page n/a, 2011.

[Tegner 12] Bengt E. Tegner, Linggang Zhu & Graeme J. Ackland. *Relative strength of phase stabilizers in titanium alloys.* Phys. Rev. B, vol. 85, no. 21, page 214106, June 2012.

[Trinité 08] Virginie Trinité, Nathalie Vast & Marc Hayoun. *Effects of localization of the semicore density on the physical properties of transition and noble metals.* Journal of Physics: Condensed Matter, vol. 20, no. 23, page 235239, 2008.

[Trinkle 03] D. R. Trinkle, R. G. Hennig, S. G. Srinivasan, D. M. Hatch, M. D. Jones, H. T. Stokes, R. C. Albers & J. W. Wilkins. *New Mechanism for the alpha to omega Martensitic Transformation in Pure Titanium.* Phys. Rev. Lett., vol. 91, no. 2, page 025701, July 2003.

[Trinkle 05] D. R. Trinkle, D. M. Hatch, H. T. Stokes, R. G. Hennig & R. C. Albers. *Systematic pathway generation and sorting in martensitic transformations: Titanium alpha to omega.* Phys. Rev. B, vol. 72, no. 1, page 014105, July 2005.

[Trinkle 06] D. R. Trinkle, M. D. Jones, R. G. Hennig, S. P. Rudin, R. C. Albers & J. W. Wilkins. *Empirical tight-binding model for titanium phase transformations.* Phys. Rev. B, vol. 73, no. 9, page 094123, March 2006.

[Troullier 91] N. Troullier & José Luriaas Martins. *Efficient pseudopotentials for plane-wave calculations.* Phys. Rev. B, vol. 43, no. 3, pages 1993–2006, January 1991.

[Vanderbilt 90] David Vanderbilt. *Soft self-consistent pseudopotentials in a generalized eigenvalue formalism.* Phys. Rev. B, vol. 41, no. 11, pages 7892–7895, Apr 1990.

[Velisavljevic 07] Nenad Velisavljevic & Gary N. Chesnut. *Direct hcp → bcc structural phase transition observed in titanium alloy at high pressure.* Appl. Phys. Lett., vol. 91, no. 10, page 101906, September 2007.

[Velisavljevic 12] Nenad Velisavljevic, Simon MacLeod & Hyunchae Cynn. *Titanium Alloys at Extreme Pressure Conditions.* In Titanium Alloys - Towards Achieving Enhanced Properties for Diversified Applications. http://www.intechopen.com, 2012.

[Verma 07] A. K. Verma, P. Modak, R. S. Rao, B. K. Godwal & R. Jeanloz. *High-pressure phases of titanium: First-principles calculations.* Phys. Rev. B, vol. 75, no. 1, page 014109, January 2007.

[Vinet 87] P. Vinet, J. Ferrante, J. H. Rose & J. R. Smith. *Compressibility of Solids.* J. Geophys. Res., vol. 92, no. B9, pages 9319–9325, 1987.

[Vohra 01] Yogesh K. Vohra & Philemon T. Spencer. *Novel gamma-Phase of Titanium Metal at Megabar Pressures.* Phys. Rev. Lett., vol. 86, no. 14, pages 3068–3071, April 2001.

[Xia 90a] Hui Xia, Steven J. Duclos, Arthur L. Ruoff & Yogesh K. Vohra. *New high-pressure phase transition in zirconium metal.* Phys. Rev. Lett., vol. 64, no. 2, pages 204–207, January 1990.

[Xia 90b] Hui Xia, G. Parthasarathy, Huan Luo, Yogesh K. Vohra & Arthur L. Ruoff. *Crystal structures of group IVa metals at ultrahigh pressures.* Phys. Rev. B, vol. 42, no. 10, pages 6736–6738, October 1990.

[Zunger 90] Alex Zunger, S.-H. Wei, L. G. Ferreira & James E. Bernard. *Special quasirandom structures.* Phys. Rev. Lett., vol. 65, no. 3, pages 353–356, July 1990.

Publications

B. E. Tegner, S. G. MacLeod, H. Cynn, J. Proctor, W. J. Evans, M. I. McMahon, and G. J. Ackland, An Experimental and Theoretical Multi-Mbar Study of Ti-6Al-4V. *MRS Online Proceedings Library*, **1269** (2011).

B. E. Tegner and G. J. Ackland, Pseudopotential errors in titanium. *Computational Materials Science*, **52**, 2–6 (2012).

B. E. Tegner, L. Zhu, and G. J. Ackland, Relative strength of phase stabilizers in titanium alloys. *Phys. Rev. B*, **85**, 214106 (2012).

S. G. MacLeod, B. E. Tegner, H. Cynn, J. E. Proctor, W. J. Evans, M. I. McMahon, and G. J. Ackland, Experimental and theoretical study of Ti-6Al-4V to 220 GPa. *Phys. Rev. B*, **85**, 224202 (2012).